ČESKÉ VYSOKÉ UČENÍ TECHNICKÉ V PRAZE
FAKULTA JADERNÁ A FYZIKÁLNĚ INŽENÝRSKÁ

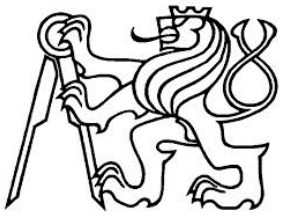

RESEARCH TASK

2017 Bc. Michal Farník

České vysoké učení technické v Praze
Fakulta jaderná a fyzikálně inženýrská

Katedra fyziky
Obor: Fyzika a technika termojaderné fúze

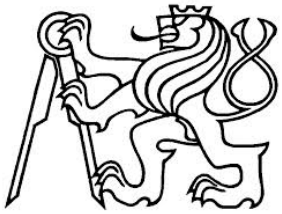

Diagnostika ubíhajících elektronů na tokamaku COMPASS pomocí EC emise

Runaway electrons diagnostics for the COMPASS tokamak using EC emission

RESEARCH TASK

Author: Bc. Michal Farník
Supervisor: Ing. Jakub Urban, Ph.D.
Year: 2017

Zadání práce

Název práce:

Diagnostika ubíhajících elektronů na tokamaku COMPASS pomocí EC emise

Autor: Bc. Michal Farník

Obor: Fyzika a technika termojaderné fúze
Druh práce: Výzkumný úkol

Vedoucí práce: Ing. Jakub Urban, Ph.D.
Ústav fyziky plazmatu, AV ČR, v.v.i

Abstrakt: Tato práce se zabývá vývojem nové diagnostiky ubíhajících elektronů na tokamaku COMPASS. Jedná se o heterodynní radiometr, který detekuje elektronovou cyklotronní záření ve vertikálním směru podél konstantního magnetického pole. Je poskytnut stručný popis fyziky ubíhajících elektronů včetně jejich generace a detekce. Následně je zde popsána teorie cyklotronní emise rychlých elektronů spolu s teorií šíření vln v plazmatu. Představeny jsou výpočty, které určili konečný design diagnostiky a pomohly v následné analýze prvních experimentálních dat. Bylo zjištěno, že lze měřit hlavně elektrony o energii 50−140 keV. Zavedená diagnostika ukazuje pozitivní první výsledky a jejich potvrzení bude předmětem další práce.

Klíčová slova: tokamak, plasma, elektronová cyklotronní emise, ubíhající elektrony, radiometer, diagnostika

Title:

Runaway electrons diagnostics for the COMPASS tokamak using EC emission

Author: Bc. Michal Farník

Abstract: This thesis deals with utilizing new runaway electron diagnostic on the COMPASS tokamak. It is heterodyne radiometer which detects electron cyclotron signal in a vertical direction along constant magnetic field. A brief intro into runaway physics is provided together with their generation and detection. Then, theory of cyclotron emission from the fast electrons and theory of wave propagation in plasma is described. Calculations which utilized final diagnostic design and helped in subsequent data analysis were presented. Possibility to measure mainly electrons with energy 50−140 keV was found. The diagnostic method shows positive first results and their confirmation will be subject of the next thesis.

Key words: tokamak, plasma, electron cyclotron emission, runaway electrons, radiometer, diagnostics

Contents

Introduction

Since the discovery of the nuclear fusion in 40's, scientists try to research this reaction for the energy gain. The difference in mass between the reactants in the form of light nuclei and products in the form of heavier nuclei and subatomic particles makes it possible. For example, the Sun and every other star exploit the process in their cores. Here on the Earth, it is much more complicated due to the probability of the reaction. The light nuclei need to overcome the Coulomb barrier. Owing to this problem, thermonuclear fusion seems to be the most promising way to build a fusion reactor.

The reactants in thermonuclear fusion gain the energy from a thermal movement. We talk about temperatures of millions Kelvins where the matter occurs in the form of the plasma. One of the ways to confine the hot plasma is using magnetic fields. The magnetic field confinement research stands before a huge crucial project called International Thermonuclear Experimental Reactor, ITER. The experimental tokamak placed in Cadarache, France has a number of objectives. ITER has been designed to confine the plasma for a longer period of time, approximately dozens of minutes, and to achieve sustained deuterium-tritium plasma. Gradual reaching these and other goals can answer many important questions and show us the feasibility of the thermonuclear power plant.

One of the problems ITER will have to deal with is high-energetic runaway electron (RE) generation. The runaway electrons present a huge threat to the tokamak device, more precisely to its first wall and internal diagnostics. These high-energy particles can be measured by various techniques. Knowledge of their position, energy and motion is essential for the effort of inhibit the presence of RE. [1]

In the first chapter of this research report will be presented an introduction to the runaway electron physics and experiments together with a description of the electron cyclotron emission (ECE) of REs. Then we focus on suprathermal ECE diagnostic used in the COMPASS tokamak. The following text will summarize experimental results and provide a comparison with simulation and further options of this diagnostic method.

Chapter 1

Runaway Electrons Physics

Runaway electrons and their effects have been subject of interests since the beginning of the plasma research on the toroidal experiments. They have been observed in early tokamak experiments in 50's and 60's due to low density discharges with many impurities. The first theoretical analysis of the runaway phenomenon was provided in 1959 by H. Dreicer.

In many toroidal fusion experiments, for example in the tokamak devices, is the plasma confinement achieved by running a current through the plasma column. A toroidal electric field is the source of this plasma current and its existence is also essential condition for a RE generation. The majority of the collisions between charged particles is managed by the long-range, small-angle Coulomb scattering. The electron collision frequency for this small-angle scattering is given by the following formula

$$\nu = \frac{n_\mathrm{e} e^4}{4\pi\varepsilon_0^2 m_\mathrm{e}^2 v^3} \ln(\Lambda), \tag{1.1}$$

where n_e is the electron density, e the elementary charge, ε_0 the vacuum permittivity, m_e and v is the electron weight and mutual velocity. The expression $\ln(\Lambda)$ stands for the Coulomb logarithm defined as

$$\ln(\Lambda) = \ln\left(\frac{\lambda_\mathrm{D}}{b_0}\right), \quad \lambda_\mathrm{D} = \sqrt{\frac{\varepsilon_0 k_\mathrm{B}}{\sum_\alpha Q_\alpha^2 n_\alpha / T_\alpha}}, \tag{1.2}$$

where b_0 is the critical collision parameter, i.e. parameter in what the scattering angle equals exactly 90°, k_B the Boltzmann constant, Q_α and T_α is the charge and temperature of the α-species particles. The λ_D in (1.2) is called Debye length.

As it can be seen, the collision frequency rapidly decreases with increasing particle energy. This is the reason why the friction force caused by collisions is not capable to compensate the influence of the induced electric force in the high-energy electrons case. These mentioned electrons are incessantly accelerated and "run away" in the velocity phase space.

Studying runaways has a numerous reasons throughout the theoretical and experimental plasma physics. Nowadays, theories that result in non-linear effects can describe REs quite successfully. On the other hand the interaction between collisionally decoupled RE and the bulk plasma is still inconsiderable. This physical effect often influences most of the complex plasma physics of tokamaks, for example the plasma transport, field perturbations impact, confinement quality and MHD instabilities. As it was mentioned earlier, runaways could represent a serious danger for the first wall of ITER and other larger tokamak facilities. It is a threat for the diagnostics inside the vacuum vessel as well. From the experimental point of view, forming an intense toroidal relativistic beam can be used for plasma heating. [2][3]

1.1 Runaway Electron Generation

Fast electron generation may have multiple causes. In the first stage of this generation we talk about runaway seed, little number of high-energetic electrons. The seed may be produced by cosmic particles, tritium decay, instabilities, Compton scattering of photons on wall atoms or resonance with plasma waves. Nevertheless, the principal processes of this so called primary mechanism are the Dreicer mechanism and the hot-tail mechanism. The secondary mechanism is based on multiplying of the generated seed by close collisions and is called avalanche mechanism.

1.1.1 Primary Dreicer Mechanism

The primary generation of runaway electrons is caused by friction force insufficient capability to compensate induced electric force. Condition for the electron acceleration in the plasma first introduced described H. Dreicer with his Dreicer field which is given as

$$E_{\mathrm{D}} = \frac{n_{\mathrm{e}} e^3}{4\pi\varepsilon_0^2 k_{\mathrm{B}} T_{\mathrm{e}}} \ln(\Lambda). \tag{1.3}$$

The Dreicer field E_{D} (in original papers [4],[5] denoted as critical field E_{c}) represents electric field in which electron velocity exceed plasma thermal velocity in one average period between collisions.

From the simplified situation it is able to derive the critical velocity and critical field formula. An electron in the plasma experiences a force equal to $\mathbf{F}_{\mathrm{e}} = -e\mathbf{E}$ and a drag force resulting from Coulomb interactions conveniently written in the form

$$\mathbf{F}_{\mathrm{d}} = m_{\mathrm{e}} \mathbf{v} \nu_{\mathrm{coll}}(v), \tag{1.4}$$

where $\nu_{\mathrm{coll}}(v)$ is the collision frequency given in (1.1). The non-relativistic movement of an electron in the direction parallel to the electric field $\mathbf{E}$ can be written as

$$m_{\mathrm{e}} \frac{\mathrm{d}v}{\mathrm{d}t} = eE - m_{\mathrm{e}} v \nu_{\mathrm{coll}}(v) = eE - \frac{n_{\mathrm{e}} e^4 \ln(\Lambda)}{4\pi\varepsilon_0^2 m_{\mathrm{e}} v^2}. \tag{1.5}$$

It is obvious that in the case of $\frac{\mathrm{d}v}{\mathrm{d}t} > 0$, electrons are accelerated due to the electric field. If there is no other force causing deceleration, generation of the electrons occurs at the critical electric field

$$E_\mathrm{c} = \frac{n_\mathrm{e} e^3}{4\pi\varepsilon_0^2 m_\mathrm{e} c^2} \ln(\Lambda). \tag{1.6}$$

At least some electrons are accelerated when the electric field is over the critical field E_c (current designation). The relation for the critical field lacks the dependence on the electron temperature and in most experiments, the value of the experimental critical field is higher [6]. The critical velocity

$$v_\mathrm{c} = \sqrt{\frac{n_\mathrm{e} e^3 \ln\Lambda}{4\pi\varepsilon_0^2 m_\mathrm{e} E}} \tag{1.7}$$

represents the threshold where the friction force equals to the electric field force.

The Dreicer mechanism of RE generation is more likely to appear for the smaller tokamak devices with larger loop voltage and lower density. There belongs the tokamak at IPP CAS v.v.i called COMPASS. In these tokamaks the electric field overcomes the critical field at least during the breakdown. Part of this runaway population could be directly released but most of it is confined [7].

1.1.2 Hot-tail Mechanism

The so called hot-tail mechanism is different from the one described above. It occurs mainly in plasma disruptions. These situations which are characterized by steep decrease of the plasma current may have multiple causes.

In the case of a radiative disruption, the most important disruption in the RE studies, sources may be the released parts of the first wall. On the other hand, we are able to induce runaways in tokamaks by injecting a high Z gas or pellets. When these impurities penetrate the plasma, there supervenes the thermal quench. The thermal electrons lose their energy owing to the ionisation and excitation of the impurity atoms, the plasma conductivity decreases and the current quench occurs. However, the fast non-thermal electrons are not decelerated due to their small collisional frequency.

The sudden plasma parameters change also changes the Dreicer field. With a lower electron temperature T_e, the value E_D considerably rises so the electric field affects only the fast collisionless electrons [8]. The hot-tail mechanism is relevant even in the case of some particular instabilities.

1.1.3 Secondary Mechanism

A condition for evolving of the secondary mechanism is an initial RE existence in the plasma. These runaways are reproduced with the high grow rate due to knock-on collisions. Take the thermal electron and fast electron close collision with a small impact parameter, in this situation a large amount of the parallel momentum is being transported. The thermal

electron gains velocity higher than the critical velocity v_c (1.7) what means it is pushed to the runaway region. This mechanism is also called "*avalanche mechanism*" because of its development character. One RE can affect several other electrons and they act as the primary ones. Energy of the created electron is about 10-20 MeV. [9]

In the present-day tokamaks with the plasma current about 1 MA, avalanche mechanism does not represent such a threat unlike in the planned large tokamak ITER. Theories end simulations predicts massive runaway formations in the ITER-like conditions (amplification factor e^{50}). It makes the avalanche mechanism the most dangerous issue in the ITER tokamak.

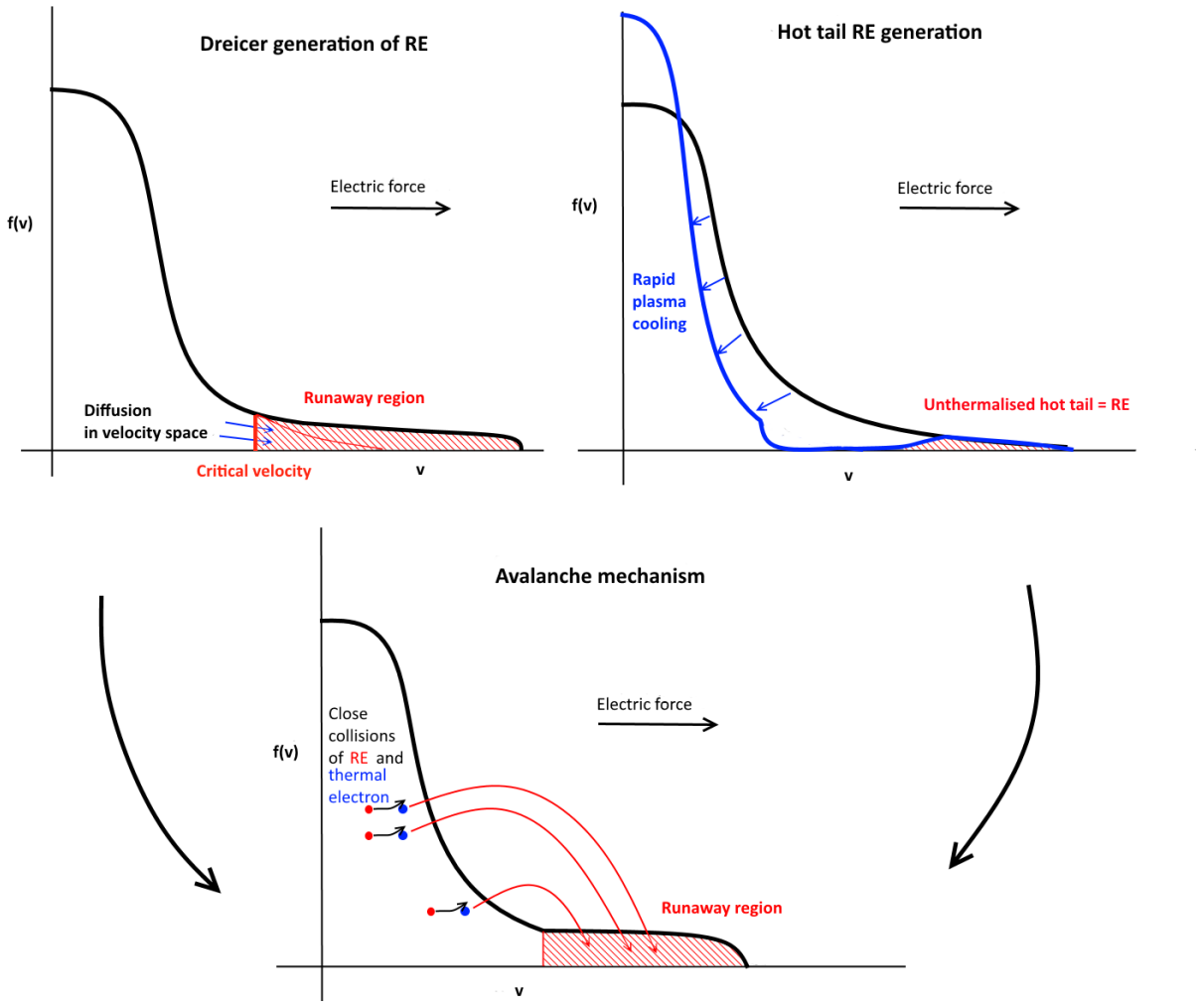

Fig. 1.1: Scheme of the RE production mechanism and its effect on the distribution function in the direction of the electric field. Used in permission of O.Ficker [7].

1.2 Principal Detection Methods

In this section the main detection approaches will be introduced. The runaway electrons diagnostic methods are divided into the two groups. The first measures consequences of the high-energetic electron impact into the tokamak first wall. The other focuses on radiative effects of the charged particle movement. The detection of the electron cyclotron emission of REs will be presented in details in the section 1.3.

Bremsstrahlung If the electron movement is not linear and uniform the electromagnetic radiation occurs. From electron-ion collisions arise the continuum radiation historically called *"bremsstrahlung"*. The kinetic energy electron loss during the collision is compensated by this radiation. For the runaway electron with relativistic velocity, the energy loss by bremsstrahlung is more substantive than the momentum loss during the collision. This radiation is detected in the soft X-ray (SXR) range of frequencies.

Synchrotron Radiation When the charged particle is placed into the magnetic field its movement is not linear and particle emits synchrotron radiation. It has the same source as the latter mentioned bremsstrahlung. The frequencies of the synchrotron radiation are in the infra red (IR) spectrum range, in the larger devices even in the visible spectrum. Using a tangentially placed fast IR camera with the line-view opposite to the plasma current may be useful for the RE synchrotron radiation measurement. With a good spatial and temporal resolution it is possible to measure the position of the beam and its change during discharge. With this diagnostic method could be someday determined the RE distribution function.

Cherenkov Radiation The electromagnetic so called Cherenkov radiation is emitted in the case of the charged particle (such as an electron) passing through a dielectric medium at the speed greater than the phase velocity of the light in that medium v_f. It is released into the shock cone, as well as the supersonic shock wave, with the axisymmetry along the direction of the particle movement with the cone angle θ given as

$$\cos\theta = \frac{1}{N\beta} \quad \text{with} \quad \beta = \frac{v_f}{c}, \tag{1.8}$$

where c is the speed of light in vacuum and N is the refractive index in the medium. The frequencies of the Cherenkov radiation are in the visible spectrum with peaks in the UV region. Cherenkov detectors contain a dense material (usually diamond, TiO2, etc.) through which can pass a relativistic electron. The emitted radiation is then converted to the electric output and amplified by the photomultiplier. The detector have to be placed inside the tokamak vessel to be sure that the electron hits the detector before any other material. It is difficult to secure the limitation of the hard X-ray photon influence. The advantages of this diagnostic method are the great spatial and temporal resolution and the ability to estimate the parallel velocity distribution function.

Interaction with the Tokamak Wall Runaways are not always well confined and some of them could be released. A fast electron then hit the limiter or the first wall. One of the possible consequences is emitting a high-energetic electromagnetic radiation with frequencies in the hard X-ray (HXR) region. In a contact with the dense matter of the first wall or limiter electrons undergo inelastic scattering on the nucleus and the electrons are strongly decelerated. They emit energy in the form of the bremsstrahlung radiation proportional to the atomic number squared Z_i^2. This process dominates for electron energies larger than 11 MeV. For electron energies under 11 MeV also takes place inelastic scattering on bounded electrons. The hard X-ray diagnostic proves the existence of REs in the plasma. With a proper calibration it is possible to estimate the distribution function, but it has to be kept in mind that there are different HXR sources as well.

The HXR photons can leave the tokamak and be measured or undergo series of absorptions and re-radiations. According to the photon energy they can even trigger some nuclear reactions. In energies about 10 MeV the collision between photon and nucleus sometimes leads to the neutron production. During the collision the nucleus experiences a giant dipole resonance ending with the fission or releasing a neutron. These neutrons are called photo-neutrons and can be measured as well. Taking into account the first wall material the most common reactions are ^{12}C(γ,n)^{11}C and ^{9}Be(γ,n)^{8}Be.

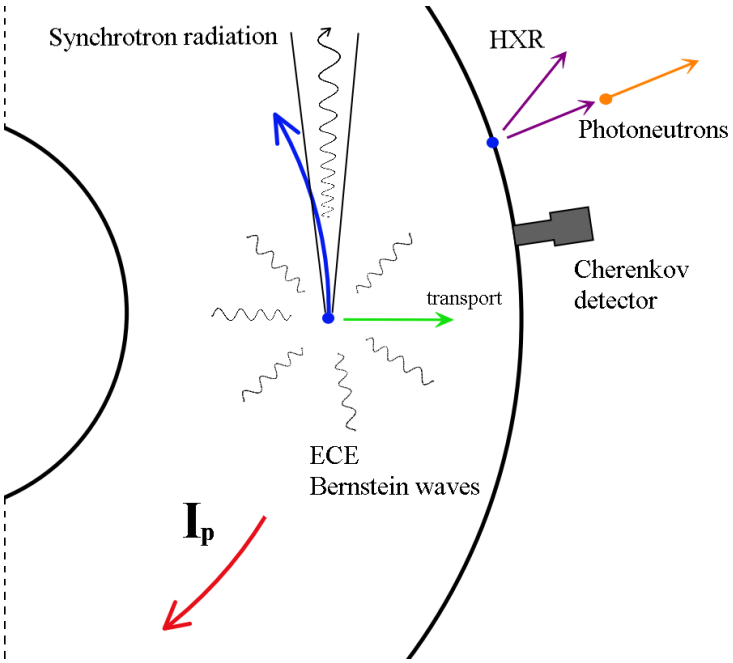

Fig. 1.2: Scheme of all kinds of RE radiation.

1.3 Electron Cyclotron Emission

The measurements used in this research task are provided by the electron cyclotron emission (ECE) diagnostic. This section will outline basics of ECE physics together with ray-tracing basics. A closer look is given at the runaway electrons cyclotron emission and its usage as a possible runaway electron diagnostic.

Every electron moving through the plasma emits electromagnetic radiation (sometimes also called *"magnetic bremsstrahlung"*) at the cyclotron frequency. Circular movement with Larmor radius along the magnetic induction line $\mathbf{B}_0$ causes this behaviour. If the electron dynamics is taken to be non-relativistic, at the first moment it may seem that the emission (or absorption) is possible only when the frequency of the emitted (or absorbed) wave is

$$\omega = \omega_{\mathrm{c}}(B) = \frac{eB_0}{m_{\mathrm{e}}}. \tag{1.9}$$

However owing to the finiteness of the Larmor radius implies that the electromagnetic field generated by an electron gyrating with the cyclotron frequency is not simply harmonic hence higher harmonics $n\omega_{\mathrm{c}}$ emerge.

Thanks to the relativistic effects, distribution function and Doppler effect, emitted frequencies have fairly wide spectrum. The frequency at which an electron, moving with a velocity $\mathbf{v}$, is able to emit or absorb waves having a wave vector $\mathbf{k}$, through the n-th harmonic contribution, is given by

$$\omega = n \cdot \omega_{\mathrm{c}}(B, v) + k_{||} v_{||} = n \cdot \omega_{\mathrm{c}}(B)/\gamma + k_{||} v_{||}. \tag{1.10}$$

The relativistic effects are represented by the well known Lorenz gamma factor, $\gamma = [1 + (p/m_e c)^2]^{1/2} = [1 -$ The second term on the right hand side denotes the longitudinal Doppler effect, the index $_{||}$ indicates the component parallel to $\mathbf{B}_0$.[10][11]

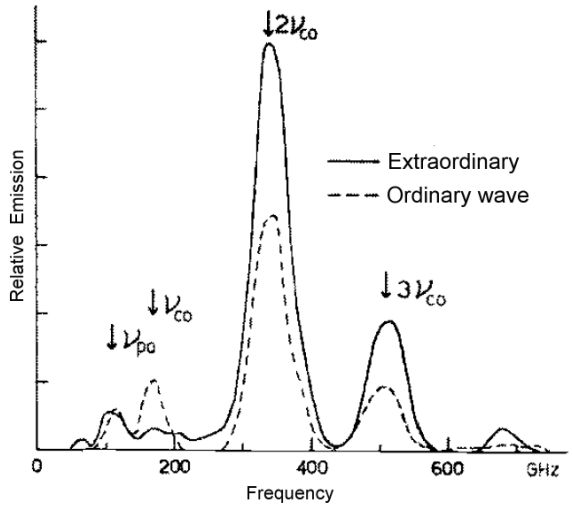

Fig. 1.3: Typical cyclotron emission spectra from a tokamak plasma when $\omega_p < \omega_c$. ν_{po} a $n \cdot \nu_{co}$ denotes the plasma and harmonic cyclotron frequency [12].

In a spatially varying magnetic field, where relativistic effects are not dominating, the emitted cyclotron frequency is proportional to the magnetic field magnitude $\omega_c = \omega_c(B)$. The fact that in tokamaks the toroidal magnetic field B_T changes with $1/R$ can be used for electron temperature measurement with a good spatial and temporal resolution. To ensure a transition of the magnetic field along the antenna line of sight, these measurements are mostly realised from the high field side (HFS) or low field side (LFS) of the tokamak. We talk about the horizontally situated ECE diagnostic (H-ECE).

1.3.1 Runaway ECE

It is possible to restrain the influence of the varying magnetic field via a vertically positioned antenna (V-ECE). The toroidal magnetic induction value becomes approximately constant along the line of sight getting only dependence on the electron velocity as shown in (1.10). In such a situation with neglecting the Doppler shift, emission at a particular frequency (ω) for a particular cyclotron harmonic (n) occurs only from electrons satisfying the resonance condition

$$\frac{\omega}{n \cdot \omega_c} = \sqrt{1 - \left(\frac{v_{||}}{c}\right)^2 - \left(\frac{v_\perp}{c}\right)^2}, \tag{1.11}$$

where $v_{||}$ and $v_\perp$ denote velocities parallel and perpendicular to the toroidal magnetic field B_T. This condition gives us a one-to-one relationship between frequency and electron energy. As a result, one can diagnose the number density and velocity anisotropy of electrons as a function of energy at the expense of returning to a chord-averaged measurement [12]. The purpose of this measurement is the fact that presence of a suprathermal population strongly affects the magnitude and the spatial location of the wave absorption.

Unfortunately antenna divergence is not negligible in many cases and $\mathbf{B}_0$ is not constant, has a poloidal component, so the Doppler effect has to be taken into account. The equation (1.11) becomes

$$\frac{\omega(c - N_{||}v_{||})}{n \cdot \omega_c c} = \sqrt{1 - \left(\frac{v_{||}}{c}\right)^2 - \left(\frac{v_\perp}{c}\right)^2}, \tag{1.12}$$

where substitution $k_{||} = \omega N_{||}/c$ is done. This entails complication into relation between the frequency and electron energy. Only emission from certain velocity phase space ($v_{||}$, $v_\perp$) fulfil the condition (1.12).

Non-thermal electrons change the cyclotron emission spectra distinctly from the one in Fig. 1.3, what can be seen in Fig. 1.4. A vital practical requirement for RE measurement is to avoid detecting multiple-reflected waves from the tokamak wall. In the analysis of the measured electron energy, a non-Maxwellian distribution function from other diagnostic or simulation code has to be utilized. For the exact value of the parallel optical index, optical depth, probability of reflections is important to count the wave propagation in plasma i. e. use the ray tracing calculations.

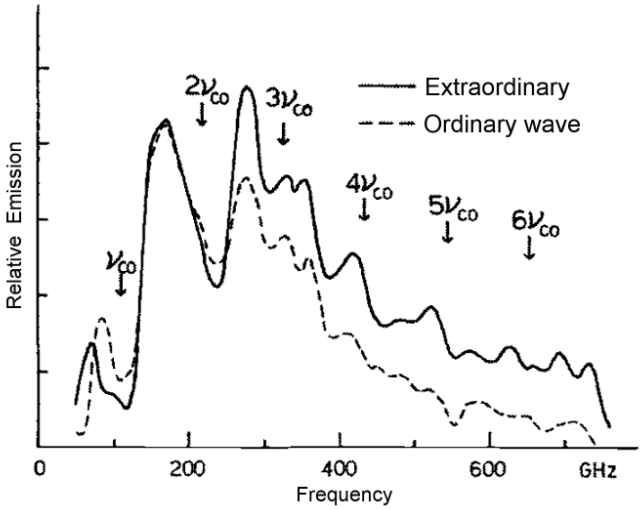

Fig. 1.4: Typical cyclotron emission spectra when significant nonthermal components exist in the electron distribution [12].

1.3.2 Wave Propagation in Plasma

For the signal analysis, we have to define important terms in theory of the wave propagation in a plasma. Generally propagating waves in a plasma follow the dispersion relation. The most common form of the disperse relation for high-frequency electromagnetic waves in a cold plasma with an external magnetic field is Appleton-Hartree formula

$$N^2 = 1 - \frac{2X(1-X)}{2(1-X) - Y^2\sin^2\theta \pm [Y^4\sin^4\theta + 4Y^2(1-X)^2\cos^2\theta]^{1/2}}. \tag{1.13}$$

where $X = (\omega_{pe}/\omega)^2$ and $\omega_{\mathrm{pe}} = \sqrt{n_{\mathrm{e}}e^2/m_{\mathrm{e}}\varepsilon_0}$ denotes the electron plasma frequency, $Y = \omega_{\mathrm{c}}/\omega$ and θ is the angle between $\mathbf{k}$ and the magnetic field $\mathbf{B}_0$. The sign in the denominator divides solution into the two modes. Solution with the + sign is called ordinary mode (O-mode), while the other is extraordinary mode (X-mode). [11]

Crucial terms in the plasma wave theory are the resonant frequency and the cutoff frequency. Cutoff is situation when refractive index goes to zero ($N^2 \to 0$) and wavelength of given wave becomes infinite. The wave is then reflected or in specific cases tunnelling occurs. In the case of resonance refractive index goes to infinity ($N^2 \to \infty$) and the wave is absorbed. In the case of extraordinary mode two cutoff frequencies appear. We talk about the right-hand (R) and the left-hand (L) cutoff.

Important cutoff frequencies for our case of the perpendicular propagation are

$$\begin{aligned}\omega_{\mathrm{O}} &= \omega_{\mathrm{pe}},\\ \omega_{\mathrm{R}} &= \left(\frac{\omega_{\mathrm{c}}^2}{4}+\omega_{\mathrm{pe}}^2\right)^{1/2}+\frac{\omega_{\mathrm{c}}}{2},\\ \omega_{\mathrm{L}} &= \left(\frac{\omega_{\mathrm{c}}^2}{4}+\omega_{\mathrm{pe}}^2\right)^{1/2}-\frac{\omega_{\mathrm{c}}}{2}.\end{aligned} \tag{1.14}$$

The resonance condition is

$$X = \frac{1-Y^2}{1-Y^2\cos^2\theta}, \tag{1.15}$$

which occurs for $\theta = \pi/2$ at the so called upper-hybrid resonance frequency

$$\omega_{\mathrm{UH}} = (\omega_{\mathrm{c}}+\omega_{\mathrm{pe}})^{1/2}, \tag{1.16}$$

where the approximation of the cold plasma fails.

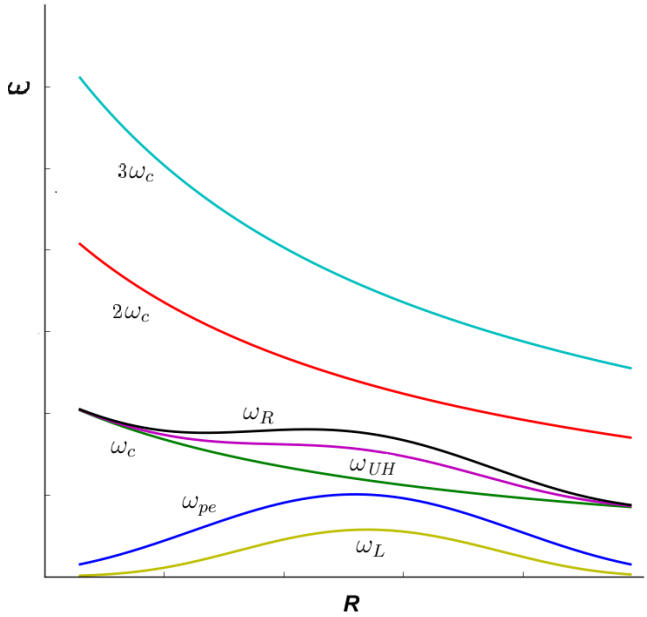

Fig. 1.5: Cyclotron, cutoff and resonant frequencies for model of a tokamak plasma ($\omega_{\mathrm{pe}} < \omega_{\mathrm{c}}$, density profile in form $n_{\mathrm{e}} = n_0 \cdot \left(1-((R-R_0)/a)^2\right)^3$

1.3.3 Ray Tracing

Tokamak plasmas are in fact inhomogeneous. In this section the geometrical optics for the wave propagation in non-homogeneous plasmas will be reviewed. The beam is considered as composed of independent rays, each propagating along a trajectory where the local dispersion relation is satisfied everywhere.

This approximation provides a elegant technique for accounting refractive effects in inhomogeneous plasmas, and plays an important role in the interpretation of measurements using electromagnetic waves [11]. In a weakly inhomogeneous plasma, properties of the medium vary in space and time. The relative change is small compared to the wavelength. As in the case of a homogeneous plasma, a non-trivial solution condition of the wave equation results in a local dispersion relation

$$\omega = \omega(\mathbf{k}, \mathbf{r}, t). \tag{1.17}$$

The ray equations then can be written in canonical form [11]

$$\begin{aligned} \frac{\mathrm{d}\,\mathbf{r}}{\mathrm{d}\,t} &= \nabla_{\mathrm{k}}\,\omega, \\ \frac{\mathrm{d}\,\mathbf{k}}{\mathrm{d}\,t} &= -\nabla_{\mathrm{r}}\,\omega, \end{aligned} \tag{1.18}$$

with ω in role of the Hamiltonian we get

$$\frac{\mathrm{d}\,\omega}{\mathrm{d}\,t} = \frac{\partial\,\omega}{\partial\,t}. \tag{1.19}$$

In the case of a known dispersion relation $D(\omega, \mathbf{k}, \mathbf{r}, t) = 0$, ray equations transform into

$$\begin{aligned} \frac{\mathrm{d}\,\mathbf{r}}{\mathrm{d}\,t} &= -\frac{\nabla_{\mathrm{k}} D}{\partial D/\partial\omega}, \\ \frac{\mathrm{d}\,\mathbf{k}}{\mathrm{d}\,t} &= \frac{\nabla_{\mathrm{r}} D}{\partial D/\partial\omega}. \end{aligned} \tag{1.20}$$

For such a medium, it is convenient to use the arc length s along the ray as a parameter and express the ray equations [13][14] in the form

$$\begin{aligned} \frac{\mathrm{d}\,\mathbf{r}}{\mathrm{d}\,s} &= -\mathrm{sgn}\left(\frac{\partial D}{\partial\omega}\right)\frac{\nabla_{\mathrm{k}} D}{|\nabla_{\mathrm{k}} D|}, \\ \frac{\mathrm{d}\,\mathbf{k}}{\mathrm{d}\,s} &= \mathrm{sgn}\left(\frac{\partial D}{\partial\omega}\right)\frac{\nabla_{\mathrm{r}} D}{|\nabla_{\mathrm{k}} D|}. \end{aligned} \tag{1.21}$$

It is not possible to neglect the absorption and emission along the trajectory as a consequence of the kinetic effects. Anti-Hermitian components appear in the dielectric tensor and the solution of the dispersion relation is a complex vector $\mathbf{k} = \mathbf{k}_{\mathrm{r}} + i\mathbf{k}_{\mathrm{i}}$. We

cogitate $|\mathbf{k}_\mathrm{r}| \gg |\mathbf{k}_\mathrm{i}|$ in the case of a plasma diagnostic. The hot plasma dispersion relation is still a 4th degree polynomial in perpendicular component of the optical index $N_\perp$

$$D = \varepsilon_{11} N_\perp^4 + P = 0, \tag{1.22}$$

where D and ε_{11} are complex and P is a polynomial of 3rd degree in $N_\perp$. If $N_\perp$ is finite and ε_{11} is nonzero the equation can be modified as

$$F \equiv \frac{D}{\varepsilon_{11}} = N_\perp^4 + \frac{P}{\varepsilon_{11}} = 0. \tag{1.23}$$

With respect to the condition $|\mathbf{k}_\mathrm{r}| \gg |\mathbf{k}_\mathrm{i}|$ we get $\mathrm{Re}\,(P/\varepsilon_{11}) \gg \mathrm{Im}\,(P/\varepsilon_{11})$ so

$$\begin{gathered} F(\omega, \mathbf{k}, \mathbf{r}, t) \approx F_\mathrm{r}(\omega, \mathbf{k}_\mathrm{r}, \mathbf{r}, t) + iF_\mathrm{i}(\omega, \mathbf{k}_\mathrm{r}, \mathbf{r}, t) + i\mathbf{k}_\mathrm{i} \cdot \nabla_{\mathbf{k}_\mathrm{r}} F_\mathrm{r} = 0, \\ F_\mathrm{r}(\omega, \mathbf{k}_\mathrm{r}, \mathbf{r}, t) = 0, \\ \mathbf{k}_\mathrm{i} \cdot \nabla_{\mathbf{k}_\mathrm{r}} F_\mathrm{r} = -F_\mathrm{i}(\omega, \mathbf{k}_\mathrm{r}, \mathbf{r}, t). \end{gathered} \tag{1.24}$$

The second equation yields the ray equations similar to (1.20)

$$\begin{aligned} \frac{\mathrm{d}\,\mathbf{r}}{\mathrm{d}\,t} &= -\frac{\nabla_{\mathbf{k}_\mathrm{r}} F_\mathrm{r}}{\partial F_\mathrm{r}/\partial\omega}, \\ \frac{\mathrm{d}\,\mathbf{k}_\mathrm{r}}{\mathrm{d}\,t} &= \frac{\nabla_\mathrm{r} F_\mathrm{r}}{\partial F_\mathrm{r}/\partial\omega}, \end{aligned} \tag{1.25}$$

and the third one gives the equation for calculating the ray absorption between two points of a ray [11]

$$\int_{s_1}^{s_2} \mathbf{k}_\mathrm{i}\,\mathrm{d}\mathbf{s} = \int_{s_1}^{s_2} \frac{|F_\mathrm{i}|}{|\nabla_{\mathbf{k}_\mathrm{r}} F_\mathrm{r}|}\,\mathrm{d}s. \tag{1.26}$$

It gets us to the radiation transfer. The equation for the radiation transfer used for the simulations is in form

$$n_r \frac{\mathrm{d}}{\mathrm{d}\,s}\left[\frac{I_\omega}{n_r^2}\right] = \beta - \alpha I_\omega \tag{1.27}$$

with the I_ω radiation intensity, α and β the absorption and emission coefficients and n_r the ray refractive index. as a result we get a parameter which is called optical depth

$$\tau = \int \alpha\,\mathrm{d}s. \tag{1.28}$$

It is crucial for a subsequent analysis of the simulations and ray tracing. To secure the vital practical requirement, avoiding detection of multiple reflections from the wall, a higher optical depth ($\tau > 1$) is needed [12]. This requirement secures conditions for thermodynamic equilibrium where Kirchhoff's law takes place as

$$I_\omega = \beta/\alpha. \tag{1.29}$$

In the presence of a significant amount of non-thermal electrons, Kirchoff's law no longer holds. Emission and absorption coefficients must be calculated separately

SPECE Code

The SPECE code [15] was developed in Instituto di Fisica del Plasma in Milan, Italy, for the analysis of the electron cyclotron emission. This code computes the solution of the equation of radiation transfer along the ray trajectories in a general tokamak equilibrium, using the cold dispersion relation, while the absorption and emission coefficients are obtained as the solution of the relevant fully relativistic dispersion relation valid at a high electron temperature. The propagation is computed by solving similar ray equations as (1.21) in form

$$\frac{\mathrm{d}\,\mathbf{r}}{\mathrm{d}\,s} = -\frac{\partial D/\partial \mathbf{N}}{|\partial D/\partial \mathbf{N}|}, \qquad \frac{\mathrm{d}\,\mathbf{N}}{\mathrm{d}\,s} = \frac{\partial D/\partial \mathbf{r}}{|\partial D/\partial \mathbf{N}|}, \tag{1.30}$$

where $D(\omega, \mathbf{N}, \mathbf{r}, t) = 0$ is cold dispersion relation for the electron cyclotron waves with ω frequency and refractive index and $\mathbf{N} = c\mathbf{k}/\omega$. SPECE uses (1.27) for computing the radiation transfer.

The magnetic equilibrium and plasma temperature and density profiles are given either analytically or numerically. Calculations can be done in Maxwellian plasma or non-thermal plasma characterized by a distribution function given by a sum of drifting Maxwellian distributions. The actual antenna pattern is simulated by means of a multi-rays calculation, using a set of m rays, uniformly distributed in radial and angular direction with respect to the antenna axis. SPECE was utilized for oblique electron cyclotron emission diagnostic at JET and can be applied on other different devices including the COMPASS tokamak or even ITER. [15]

Chapter 2

Suprathermal ECE Diagnostics

2.1 Realized Experiments at Other Devices

Experiments using ECE to determine a non-Maxwellian part of a electron velocity distribution function was implemented. A significant amount of them has focused on electron electron heating (ECRH), lower hybrid heating (LHRH) or electron cyclotron current drive (ECCD) influence. We will present selected experiment in the following section.

2.1.1 TCV

On the TCV tokamak, measurements of ECE from the high field side (HFS) with plasma heated by the second (X2) and third harmonic X-mode (X3) ECRH and ECCD was realized.

To measure suprathermal electron parameters, TCV has been equipped with a ECE radiometer working in the second harmonic frequency range of the X-mode with two possible receiving antennae on the HFS. In case of the antenna placed on the LFS the non-thermal ECE, which is relativistically frequency down-shifted, went through the thermal EC resonance region and was reabsorbed if the plasma was optically thick. The ECE was then thermal and information about non-thermal electrons was lost. Antenna on the HFS observed a down-shifted radiation without absorption at the thermal resonance.

The 24 channel heterodyne radiometer has been used and covers the frequency range $78-114$ GHz. The bandwidth of the each channel was 750 MHz, corresponding to the radial resolution between 0.4 cm (edge) and 1 cm (centre) with respect to the cold resonance.

Conclusion of this measurement was that high power X2 ECCD and/or X3 ECRH injection creates a suprathermal electron population whose ECE can be measured bz antenna on the HFS of the tokamak. It has been shown that the radiometry in such a configuration is very sensitive to the non-thermal ECE. Under the assumption that the electron distribution function is a linear combination of two Maxwellians, the first one describing the bulk and the second one the suprathermal population, the resulting ECE can be described by a superposition of the bulk and suprathermal emissions. [16]

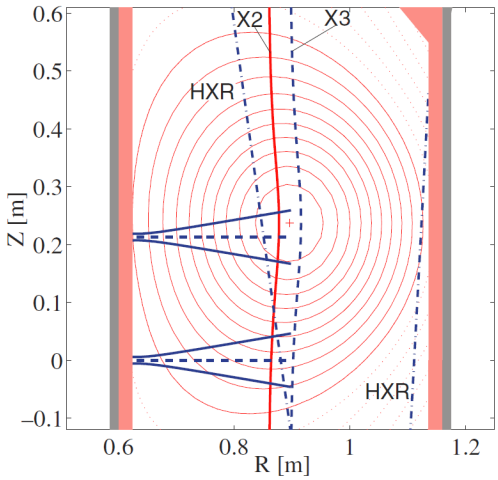

Fig. 2.1: Poloidal view of TCV with the antenna patterns of the two lines of sight of the radiometer and the two cold resonances of the gyrotrons X2 (vertical full line) and X3 (vertical dashed line). The two dash-dotted lines show the innermost and outermost chords of the HXR camera. Taken from [**?**].

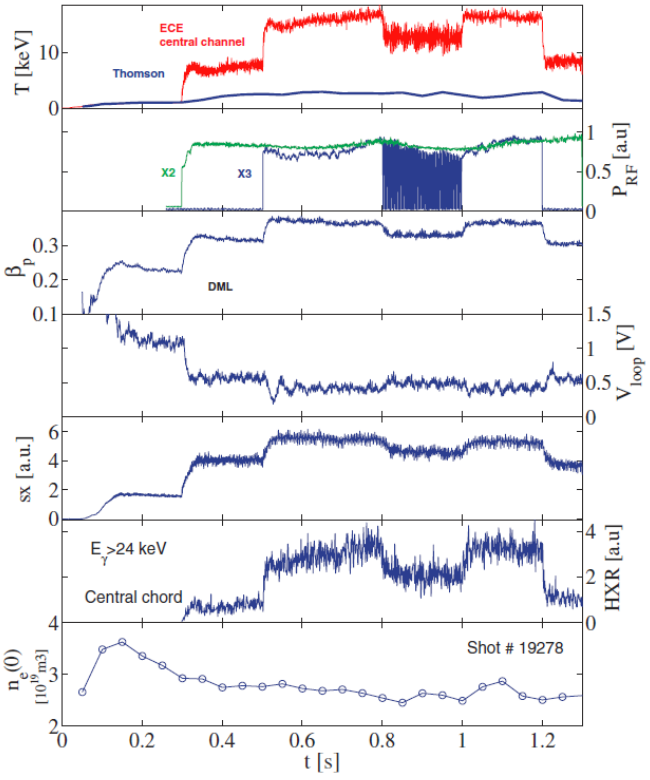

Fig. 2.2: Temporal evolution of different plasma parameters for the EC heated plasma #19278 with 480 kW central X2 CO-ECCD+20° and 450kW central X3 ECH. From top to bottom: (1) ECE and Thomson temperatures T_{TS}; (2) RF power for X2 and X3 ECH; (3) poloidal beta; (4) U_{loop}; (5) SXR signal; (6) HXR signal with photon energies $E_\gamma > 24$ keV; (7) central electron density obtained by TS. Taken from [**?**].

2.1.2 Alcator C

As it was said before the ECE measured vertically through the line of constant magnetic field could yield detailed information about the electron velocity distribution. The diagnostic developed for this purpose on the Alcator C tokamak used the rapid-scan polarizing Michelson interferometer InSb detector system for the spectrum measurement. It was utilized for the determination of the nonthermal electron velocity distribution of lower hybrid radio-frequency heating (LHRH) plasmas.

The major difficulty with the V-ECE measurements is the suppression of multiply reflected and depolarized beams from entering the antenna. This occurs at the metallic vacuum chamber wall. To eliminate this unwanted signal, a well-collimated emission collecting system and a compact, vacuum-compatible submillimeter viewing dump, have been employed at the Alcator C tokamak. The optical system for the ECE spectra measurement had the frequency range 100−900 GHz and is shown in Fig. 2.3.

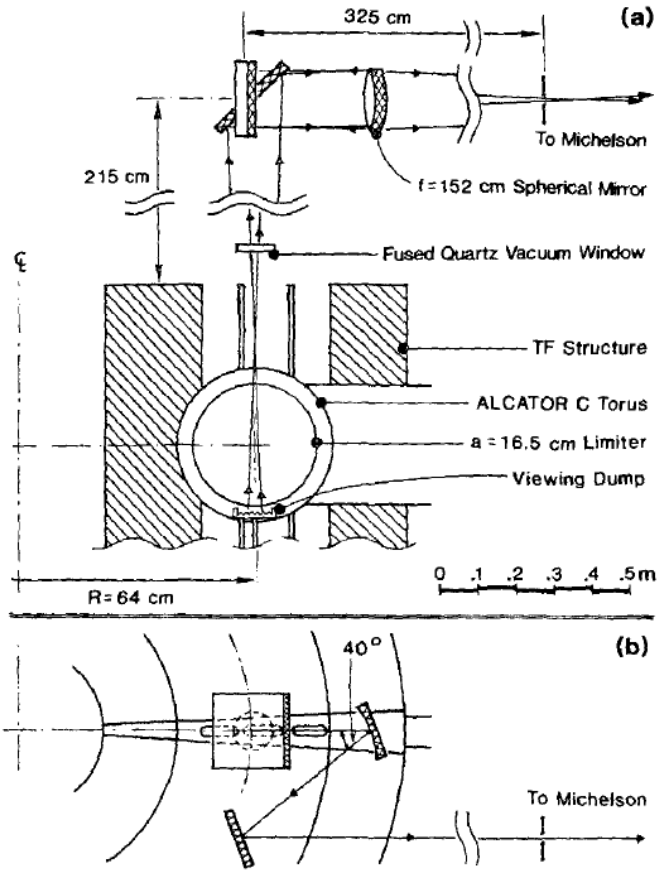

Fig. 2.3: Scaled scheme of elevation (a) and plan (b) views of the optical system. Taken from [?].

In Fig. 2.4 can be seen the two ECE spectra, one before the radio-frequency pulse, and another, a typical spectrum during LHRH at a density of $n_e = 0.7 \cdot 10^{20}$ m^{-3}. The nonthermal spectrum shows several important features. The down-shifted first harmonic emission is seen below 220 GHz. The drop at 220 GHz is due to the thermal plasma absorption. The peak at 270 GHz is consequence of the right-hand cutoff. The dips at 380 and 560 GHz are atmospheric water-vapour absorption lines.

The distribution function parameters were deduced in the energy range 50−230 keV by use of computer code which takes into account the mild harmonic overlap. The estimate of the energetic electron population density is $10^{-3} \cdot \overline{n}_e$ in given range. [17][18]

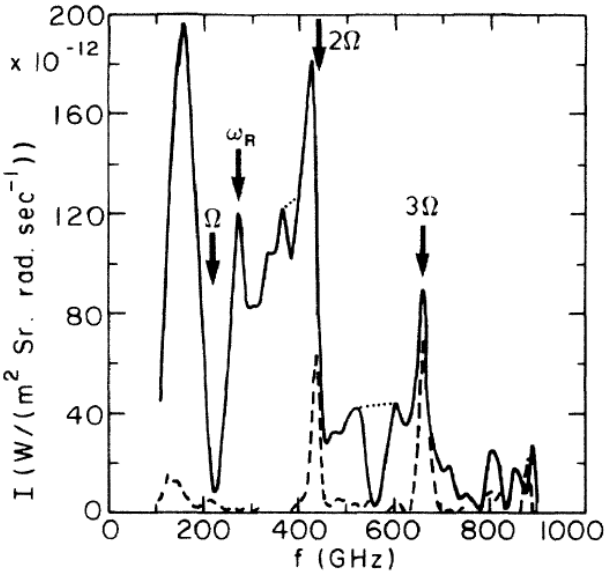

Fig. 2.4: X-mode ECE spectra for nonthermal emission LHRH shown by the solid line, and thermal emission just prior to injection of the same discharge shown by the broken line. Taken from [18].

Similar experiments were made for example on TEXT-U [19], TFTR [20], HT-7 and DIII-D [21]. None of them has investigated electron cyclotron emission of the runaway electron population.

2.2 COMPASS Experimental Setup

The heterodyne radiometer is used for the ECE diagnostic on the COMPASS tokamak. Its main focus was to measure so called electron Bernstein mode emission (EBE) [22]. These are quasi-electrostatic EC modes, which do not suffer from high density limitations.

The radiometer consists of the separated front-end and 16-channel intermediate frequency (IF) receiver with the bandwidth 1.5−15 GHz. Each channel has a second mixer stage, a digitally controlled built-in attenuator 0−30.5 dB in 0.5 steps, a power detector, and a DC amplifier, which provides a linear output voltage of 0–10 V. 0−10 V / DC−1 MHz and the bandwidth 850 MHz. The system shown in Fig. 2.5 contains the front-end with Ka-band (26.5−40 GHz) or E-band divided into two subbands (60−74.5 GHz/76.5−90 GHz). The receiver uses a perpendicular vacuum chamber port. Horn antenna is placed behind a silicon port window as it is shown in Fig. 2.6. [22][23]

In the measurements analysed in this work, E2-band (76.5−90 GHz) is used. The reciever has only 13 channels due to the channel 12,15 and 16 defects. The effective range of the COMPASS ECE diagnostic with E2-band attached is 76.5−88.3 GHz. No calibration during these experiment was utilized.

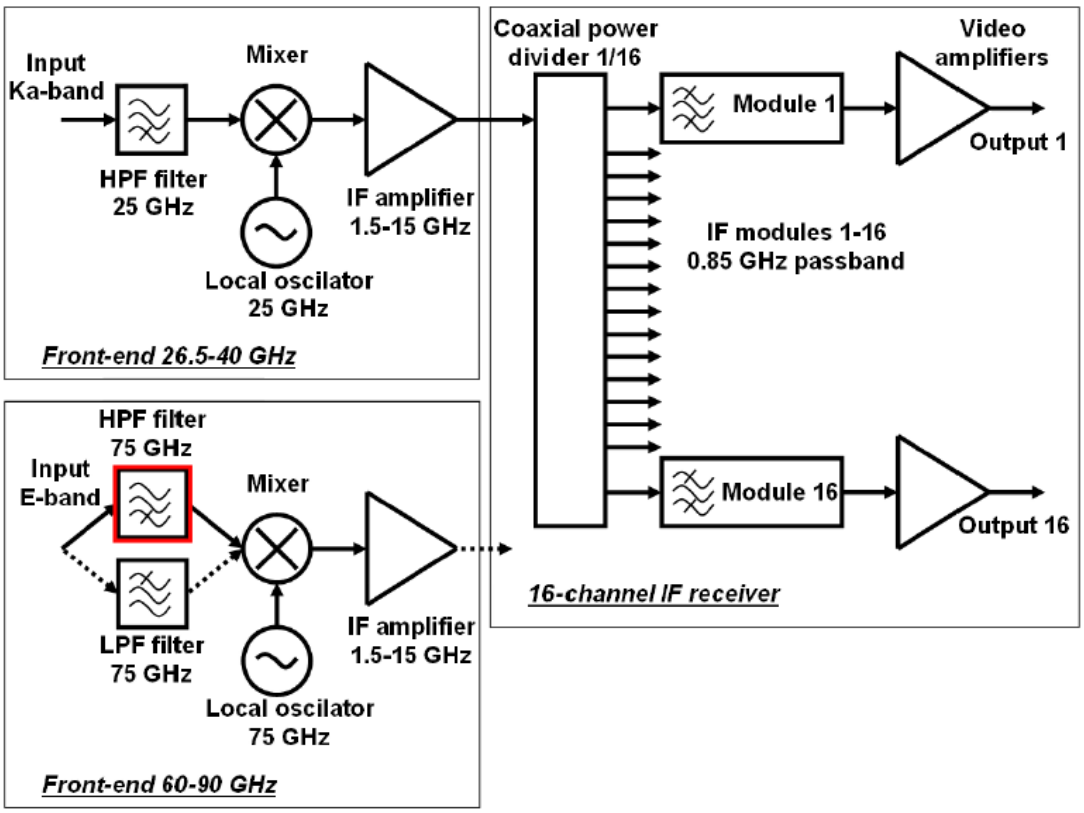

Fig. 2.5: Block scheme of EBE/ECE radiometer for COMPASS. Taken from [22].

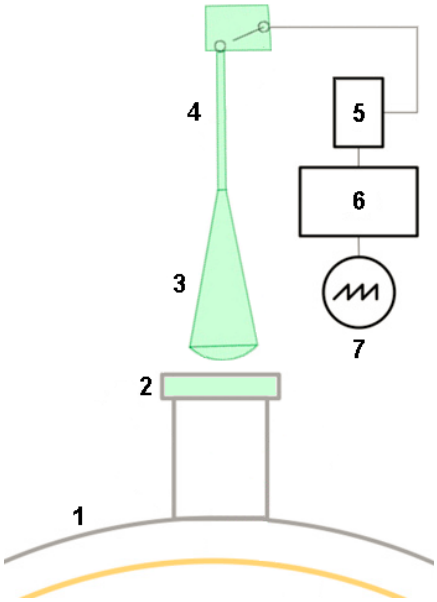

Fig. 2.6: Scheme of the antennae setup. (1) COMPASS vessel; (2) vacuum silicon port window; (3) horn antennae; (4) waveguide; (5) front end; (6) IF receiver; (7) digital oscilloscope

Chapter 3

Experimental Results

3.1 Simlulations and calculations

Now we present simulation results, which have been used for utilizing final design of the diagnostic and for data interpretation. The first thing to be investigated is a presence of cutoffs. The cutoff frequencies (1.14) increase with the electron plasma frequency ω_{pe} which is dependent on the electron density $\omega_{\mathrm{pe}} \sim \sqrt{n_{\mathrm{e}}}$ and it is favourable to choose front-end as high as possible to be able measure in highest possible plasma densities. In the Tab. 3.1 are shown electron densities for $B = 1.15$ T, i.e. in the centre of the COMPASS tokamak during a typical discharge. If the density value is below the shown number, the measured wave is not limited by the cutoff area anywhere during its propagation through the whole plasma. In the case of the Ka-band in frequencies higher than 30 GHz we find ourselves slightly above the electron cyclotron frequency and the right-hand cutoff reflects the waves on the very edge of the plasma. This band is therefore worthless for the intended experiment.

	ν [GHz]	n_{eO} [10^{19} m^{-3}]	n_{eX} [10^{19} m^{-3}]
Ka-band	26.5	0.87	1.89
	38.3	1.82	0.29
E1-band	61.7	4.72	2.26
	74.5	6.89	3.91
E2-band	76.5	7.26	4.21
	88.3	9.67	6.15

Tab. 3.1: Cutoff electron densities of the O-mode (n_{eO}) and X-mode (n_{eX}) for the given front-end boundary frequencies ν in the plasma centre.

The most advantageous possibility is to choose the E2-band with the highest frequencies. It is able to measure O-mode and X-mode waves at frequencies not limited by cutoff in case of low density discharges, which are conducted on the COMPASS tokamak during

runaway electron campaign. We talk about discharges with the intended line-averaged electron density $\overline{n}_{\mathrm{e}}$ in the range $1 - 3 \cdot 10^{19}$ m^{-3}.

Electron kinetic energies (momentum) as well as the velocity phase space which fulfil the resonance condition can be determined from the range of frequencies with use of (1.12). As it was mentioned earlier, the emitted cyclotron frequency is down-shifted with electron reaching relativistic velocity. Along the line of constant magnetic field $B = 1.15$ T the cyclotron frequency has value $f_{\mathrm{ce}} = 32.2$ GHz. It yields the fact that it is possible to measure down-shifted radiation from third and higher harmonic cyclotron frequency. The Fig. 3.1 and Fig. 3.2 show the velocity phase space (+) for the resonance condition and the kinetic energy (•) relevant to the plotted point of the phase space for 3$^{\mathrm{rd}}$, 4$^{\mathrm{th}}$ and 5$^{\mathrm{th}}$ harmonic frequency.

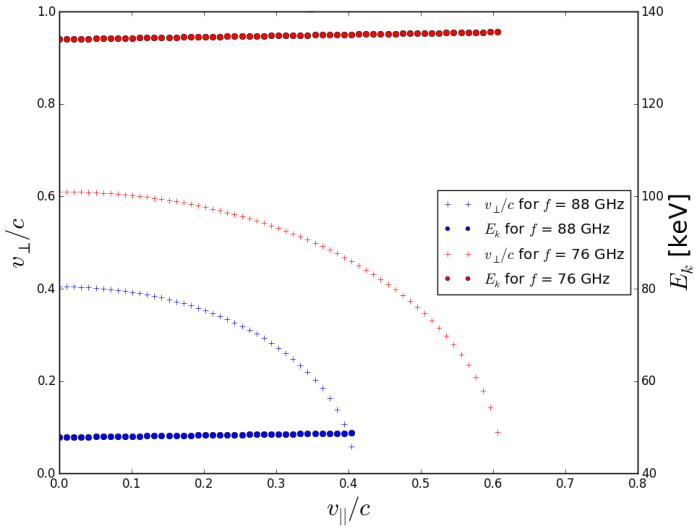

Fig. 3.1: Solution of the resonance condition with value of the electron kinetic energy E_k for $N_{||} = 0.004$ and emission from 3$^{\text{rd}}$ harmonic for boundary E2-band frequencies.

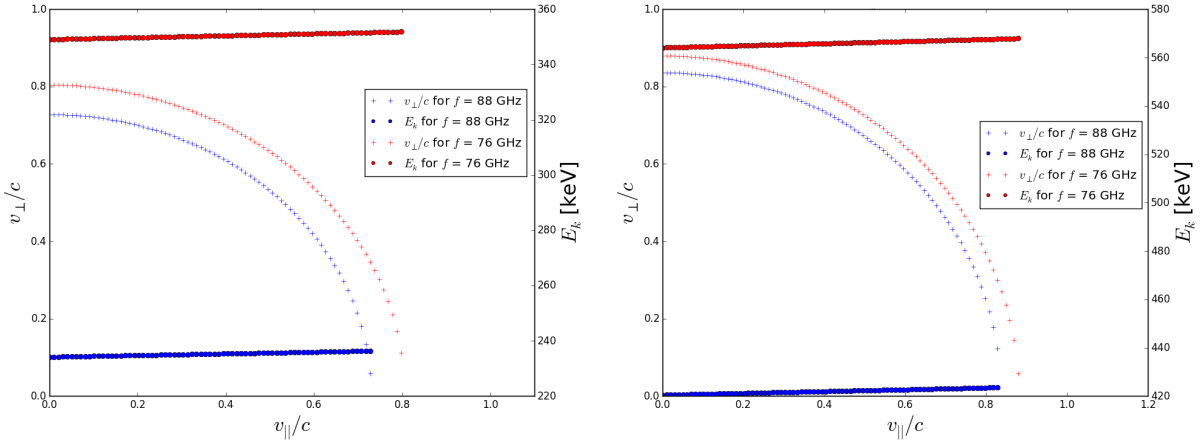

Fig. 3.2: Solution of the resonance condition with value of the electron kinetic energy E_k for $N_{||} = 0.004$ and emission from 4$^{\text{th}}$ (left) and 5$^{\text{th}}$ (right) harmonic for boundary E2-band frequencies.

From the brief look at the shown figures we are able to determine the electrons that can emit the radiation that is V-ECE diagnostic with E2-band attached capable of measuring. These are $50 - 140$ keV, $230 - 350$ keV and $420 - 570$ keV therefore it is able to investigate low-energy REs with parallel velocities above 0.4 c. We can call electrons in this phase space "runaway" because of the critical velocity value maximum $v_{\text{c}} = 0.34$ c which corresponds to the kinetic energy $E_{\text{ck}} = 35$ keV. It is essential to keep in mind that the higher harmonic used the lower radiation intensity emitted as same as shown in Fig. 1.4.

The third thing to be investigated is wave mode suitability for the measurement, i.e. optical depth values for O-mode and X-mode. In Maxwellian plasma there is low number

of the resonant electrons, therefore neither absorption nor emission, in the centre along the line of constant magnetic field B_0 in the measured frequency range $76.5 - 88.3$ GHz. This fact is favourable for measurement of runaway electrons. It is necessary to add a non-thermal component into the simulation to count the absorption coefficient and then optical depth. The simplest way is to use bi-Maxwellian plasma. The added non-thermal component is in the SPECE code characterized by the velocity $u_{\max} = p/mc$ at the end of the tail plateau, by the temperature T_{tail} and distribution function

$$\eta = \frac{n_{\text{e,tail}}}{n_{\text{e,bulk}}} = \eta_0 \exp\left[-\left(\frac{\psi - \psi_0}{\psi_{\text{c}}}\right)^2\right]. \tag{3.1}$$

Values of η_0, ψ_0 and ψ_{c} have to be chosen. For the sake of simplicity, assume runaway electron presence only in the center of the plasma. This assumption gives $\psi_0 = 0$. The width of the spatial distribution function could be chosen as $\psi_{\text{c}} = 0.1$. A number of runaways can be roughly estimated from the measured RE current as

$$N_{\text{RE}} = \frac{2\pi RI}{ec}$$

In COMPASS runaways constitute at most thousandth of all electrons present in the plasma in the low-density discharge. This gives us simplified equation

$$N_{\text{RE}} = \int_{\psi=0}^{\psi=1} n_{\text{e,tail}} \cdot \mathrm{d}V = n_{\text{e,bulk}} \sum_{\psi} \eta \Delta V_\psi = n_{\text{e,bulk}} \eta_0 \sum_{\psi} \exp\left[-(10 \cdot \psi)^2\right] \Delta V_\psi \approx 1 \cdot 10^{16}$$

and the solution

$$\eta_0 = \frac{1 \cdot 10^{16}}{n_{\text{e,bulk}} \cdot \sum_\psi \exp\left[-(10 \cdot \psi)^2\right] \Delta V_\psi}. \tag{3.2}$$

Together with modified n_{e} and T_{e} profiles from the shot #13127 and choice of $u_{\max} = 0.4$ and $T_{\text{tail}} = 60$ keV to fit resonant parameters from Fig. 3.1 we get $\eta_0 = 0.015$. Density profile was multiplied by constant to get profile with maximal density in the center of the plasma $n_{\text{e,max}} = 3 \cdot 10^{19}$ m^{-3} and secure no limitations by cutoffs. Profiles are in Fig. 3.3.

Optical depth can now be evaluated for O-mode and X-mode. This particular simulation can be seen in Fig. 3.4. Values of the optical depth for X-mode are 20 times higher than for O-mode.

During the evaluation of various simulations this difference between values of the optical depth stayed almost the same. As it was mentioned earlier, the goal is to prevent detection of reflected from the tokamak wall. In the case of $\tau > 1$ reflections are negligible but unfortunately parameters of the plasma and available radiometer on the COMPASS tokamak do not provide suitable conditions. Choice of X-mode polarization is still advantageous, however data analysis is going to be considerably onerous.

For the first measurement of the V-ECE diagnostic of the runaway electron was chosen E2-band with frequency range $76.5 - 88.3$ GHz with X-mode polarization. At this moment it is possible to check trajectories in dependence on the cutoff presence what is shown in Fig. 3.6.

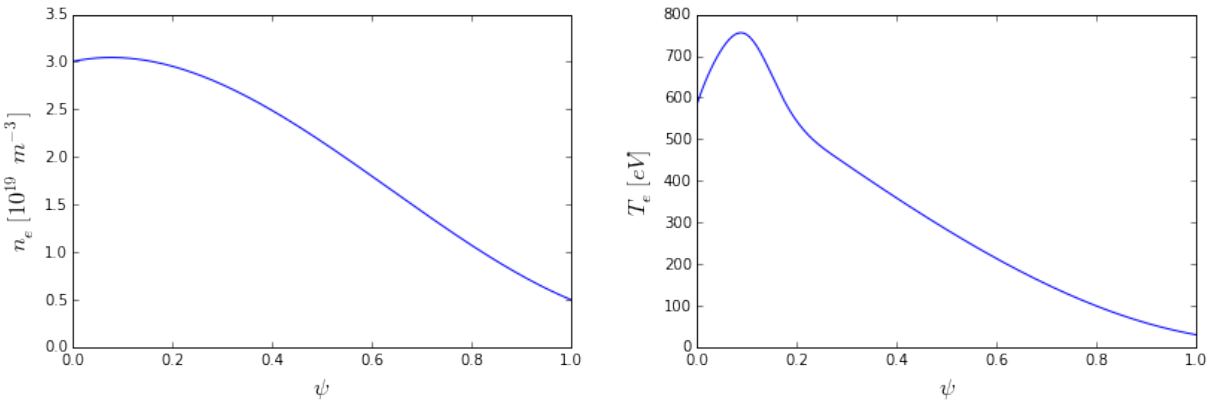

Fig. 3.3: Used electron density and temperature profiles from TS.

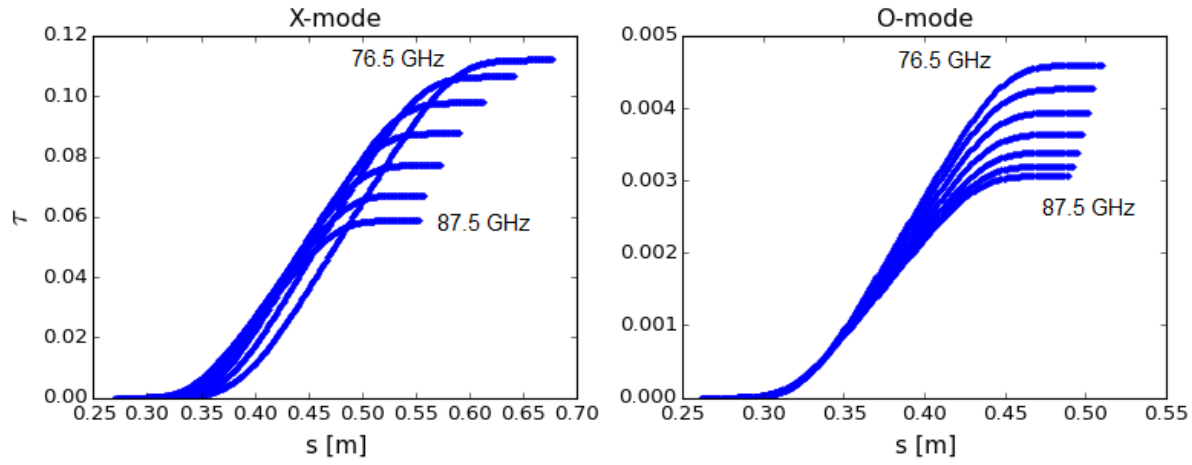

Fig. 3.4: Values of the optical depth τ in dependence on ray path length s for both O-mode and X-mode for odd E2-band channels.

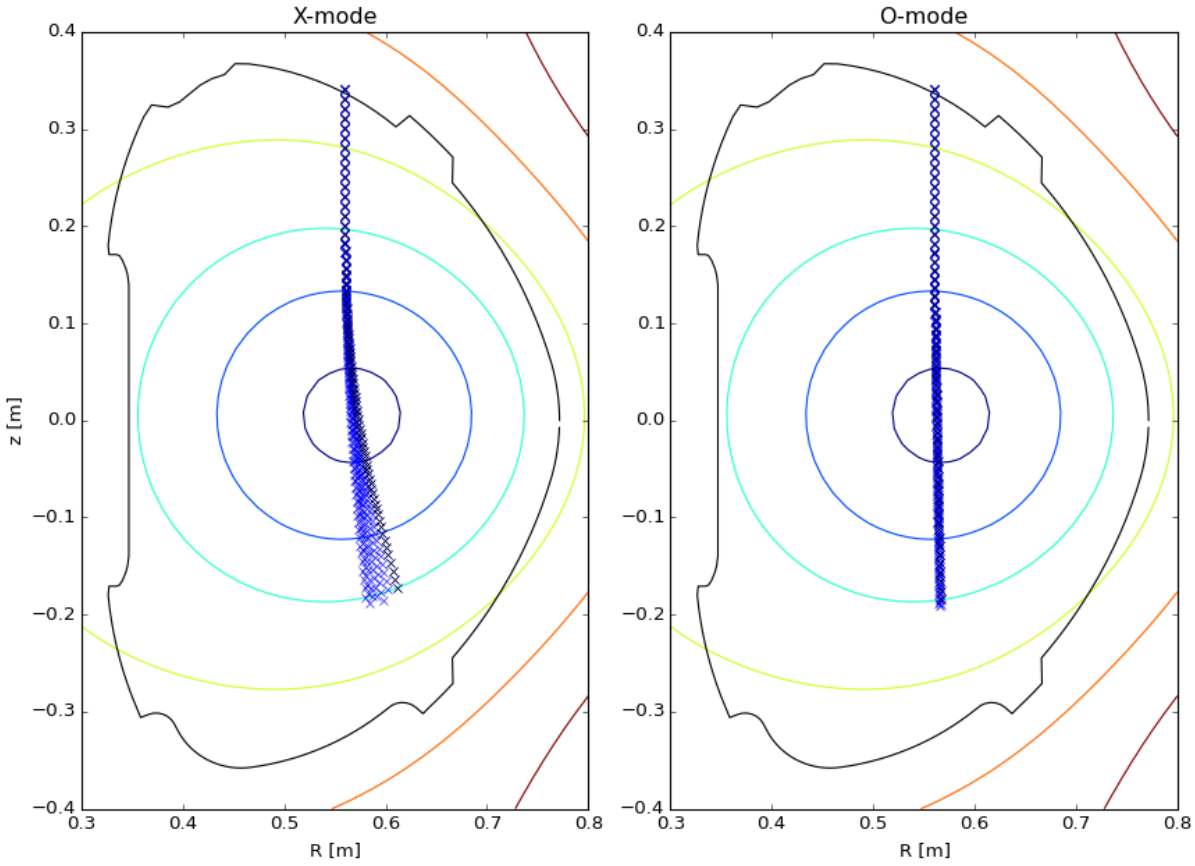

Fig. 3.5: Poloidal view of the trajectories of the O-mode and X-mode ray in the COMPASS tokamak, profiles from Fig. 3.3, frequencies 76−88 GHz.

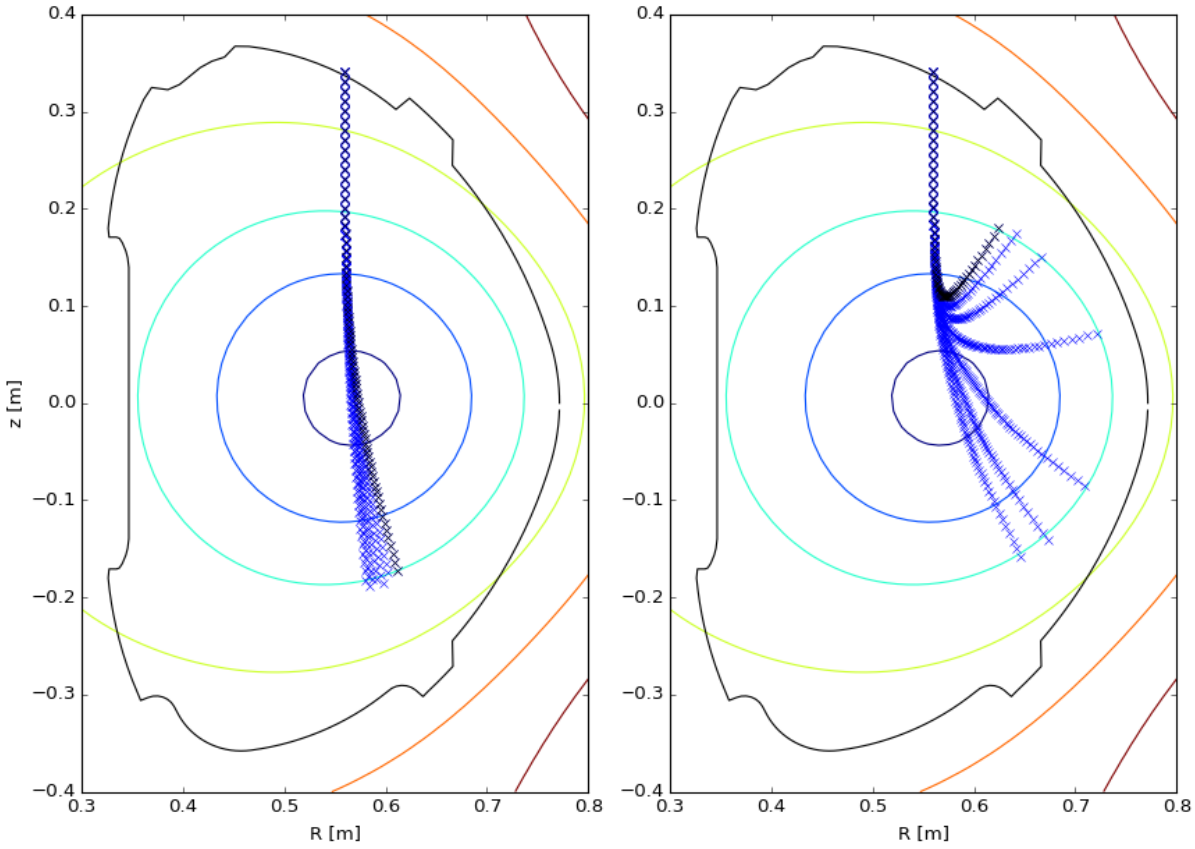

Fig. 3.6: Poloidal view of the trajectories of the X-mode ray with maximum electron density in the center of the plasma $n_{\mathrm{e,max}} = 3 \cdot 10^{19}$ m^{-3} ($\overline{n}_{\mathrm{e}} = 1.75 \cdot 10^{19}$ m^{-3}) and $n_{\mathrm{e,max}} = 5 \cdot 10^{19}$ m^{-3} ($\overline{n}_{\mathrm{e}} = 3 \cdot 10^{19}$ m^{-3}).

3.2 First Experimental Results

COMPASS is a small machine with a relatively high loop voltage U_{loop}. REs are usually generated in the rump-up phase and could be driven or released by MHD instabilities. For the purpose of data analysis discharges from the 12/2016 Runaway campaign on the COMPASS tokamak are used. These are experiment with low-density plasma focused on various RE studies. These studies include:

- Runaway electron presence in the flattop phase of low-density discharges.
- Disruptions with RE beam generation using high Z impurity massive gas injection (MGI) to terminate the thermal plasma.
- Interaction of REs with magnetic-hydrodynamic (MHD) active plasma also using resonance magnetic perturbations (RMPs).

Discharges shown in this thesis are among the first two cases. Measurements are not calibrated. In the next figures first channel (ch1 - 76.5 GHz) is shown if it is not said otherwise.

3.2.1 Dependence of V-ECE Signal on Density

First thing to be investigated is ECE from high-density signal without non-thermal electrons. This experiment is able to ascertain existence of spurious signal. A discharge with density higher than cutoff condition, i.e. line averaged density $\overline{n}_{\text{e}} = 5 \cdot 10^{19}$ m^{-3}, is chosen and shown in Fig. 3.7. Noise level signal was measured during flattop phase of this discharge what means unwanted signal did not appear. The value of the critical velocity is $v_{\text{c}} = 0.34$ c for this shot.

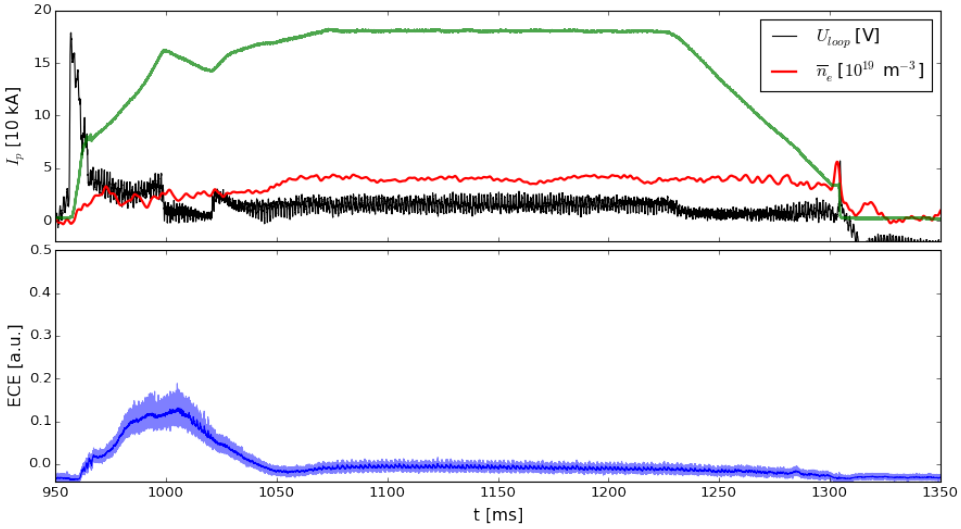

Fig. 3.7: Plasma current I_{p}, loop voltage U_{loop}, line averaged density $\overline{n}_{\text{e}}$ and ECE signal of the shot #13086.

In the shots with $\overline{n}_e < 2.8 \cdot 10^{19}$ m^{-3} and no cutoff limitations shown in Fig. 3.8 REs arise what is evident in signal of the HXR diagnostic. Presumably the signal from V-ECE radiometer hails principally from runaway electrons. The critical velocity value from (1.7) confirms that idea. The value is below 0.27 c for these discharges. Comparison with latter mentioned HXR serves us as an evidence. In the rump-up phase of the discharge an ECE peak can be seen as well as belatedly peak in HXR signal. It corresponds to the occurrence of the primary generation, so called runaway seed, which is poorly confined and most of the REs from this seed interacts with the first wall producing HXR. The decreasing signal amplitude can be attributed to RE losses during the discharge.

From the analysis in chap. 3.1, an apparently low value of the optical depth occurs. In virtue of this problem more precise analysis taking reflections from the vacuum vessel into account has to be done. For the sake of reliability it is planned to calculate a correlation function between V-ECE and HXR signal from the runaway seed.

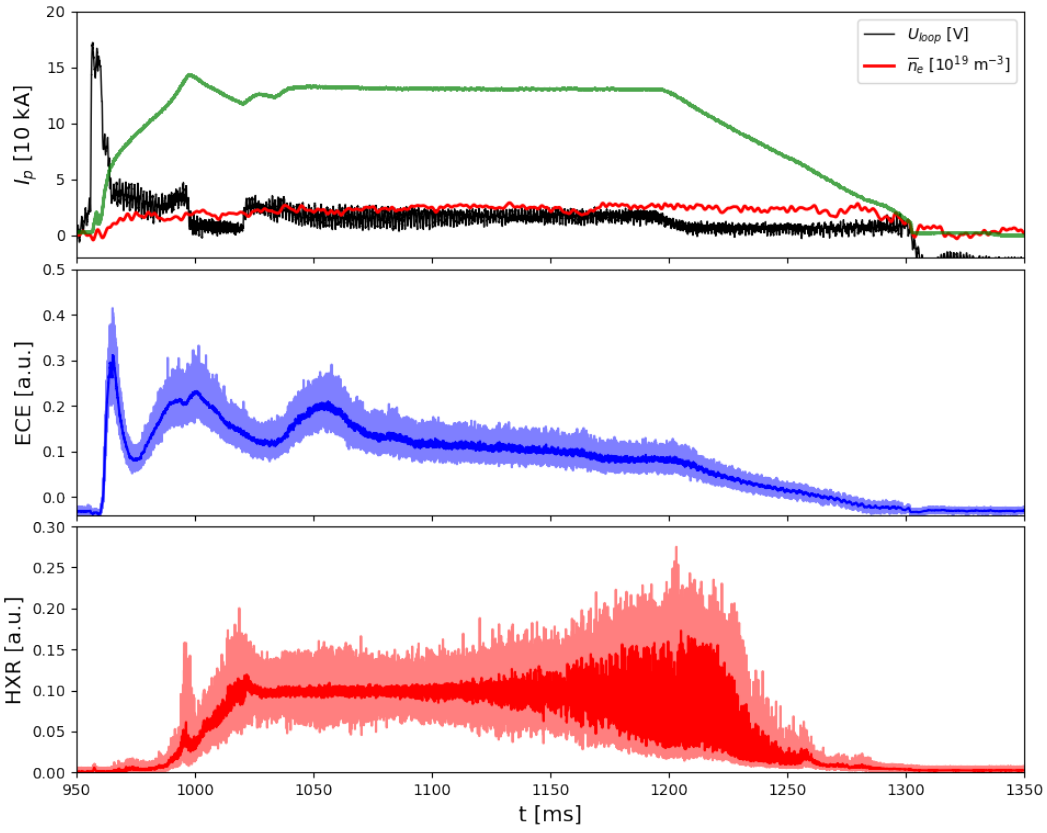

Fig. 3.8: Data from diagnostics with HXR signal, shot #13065. Dark line is the smoothed signal

As the last example in this section we will analyse a very low-density discharge. In Fig. 3.9 such a shot can be seen. Densities in these experiments are below $1.8 \cdot 10^{19}$ m^{-3}. This analysis is necessary due to a strange behaviour of the ECE signal. It clearly does not reflect only RE presence and does correlate only with electron density fluctuations. The ECE signal is in addition to previous cases 10 times stronger.

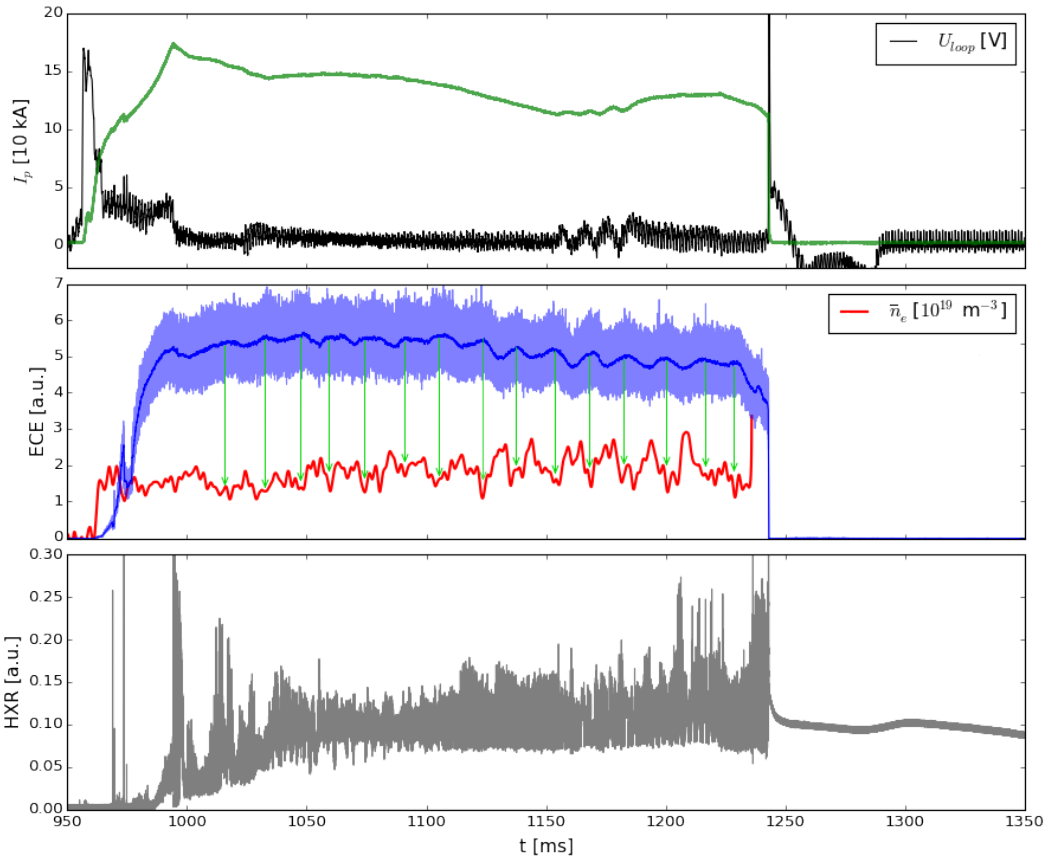

Fig. 3.9: Data from diagnostics, shot #13091. Visible corelation between line averaged density $\overline{n}_\mathrm{e}$ and ECE signal.

One of the explanation could be an optical depth threshold. When the density and also the optical depth decreases, the discussed reflections from the tokamak wall appears. The fact that the difference from ECE signal in Fig. 3.8 to signal in Fig. 3.9 is not gradual but sudden together with signal magnitude difference proves this theory wrong.

The sudden increase implies an existence of another radiation source. It might be regions of thermal cyclotron emission from the 2$^{\mathrm{nd}}$ (HFS) and 3$^{\mathrm{rd}}$ (LFS) harmonic. Their position is visualised in Fig. 3.10 and Fig. 3.11.the beams are substantially deflected to the LFS, but no thermal emission from 3$^{\mathrm{rd}}$ harmonic is observed even when densities are slightly below cutoff limit. It leads us to an idea that there exists a density threshold where the emission from the 2$^{\mathrm{nd}}$ harmonic (HFS) is able to reach the receiving antenna. To prove this idea, a full-wave simulation of the reflection is going to be utilized.

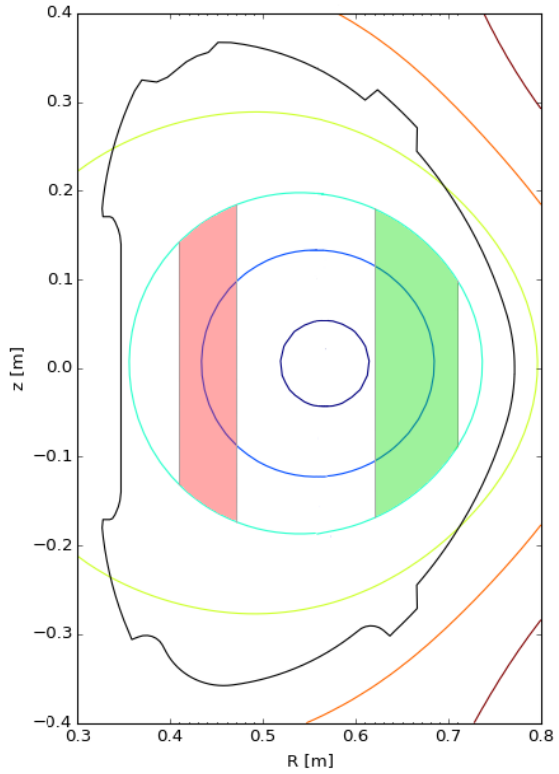

Fig. 3.10: Thermal ECE regions in plasma. Red: 2nd harmonic; Green: 3rd harmonic.

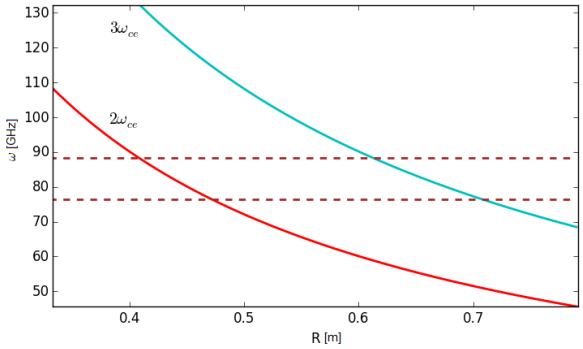

Fig. 3.11: Thermal ECE regions in plasma for E2-band and $B = 1.15$ T

3.2.2 V-ECE and Presence of the REs

To validate the measurement of the ECE from the runaways, a comparison of two analogous discharges will be presented. The only difference between the shot in Fig. 3.12 and the one in Fig. 3.13 is the amount of the RE population. As an indicator of a RE presence the HXR signal can be used.

Runaways can be affected by the gas-puffs and density in the rump-up phase. The runaway seed is then distinctly suppressed and the RE population is lower. It is never fully removed. The weakness of the signal in the case with low RE population is also the proof of not measuring thermal emission from the 3^{rd} harmonic region on the low field side of the plasma. Signals at the end of the both shots are alike due to the lack of the low-energy RE at the time.

From the first measurement we can suggest in suitable discharges electron cyclotron emission from the runaway electron can be measured and analysed. Regarding to lack of the calibration, number of the REs or evolution of the RE distribution function could not be determined.

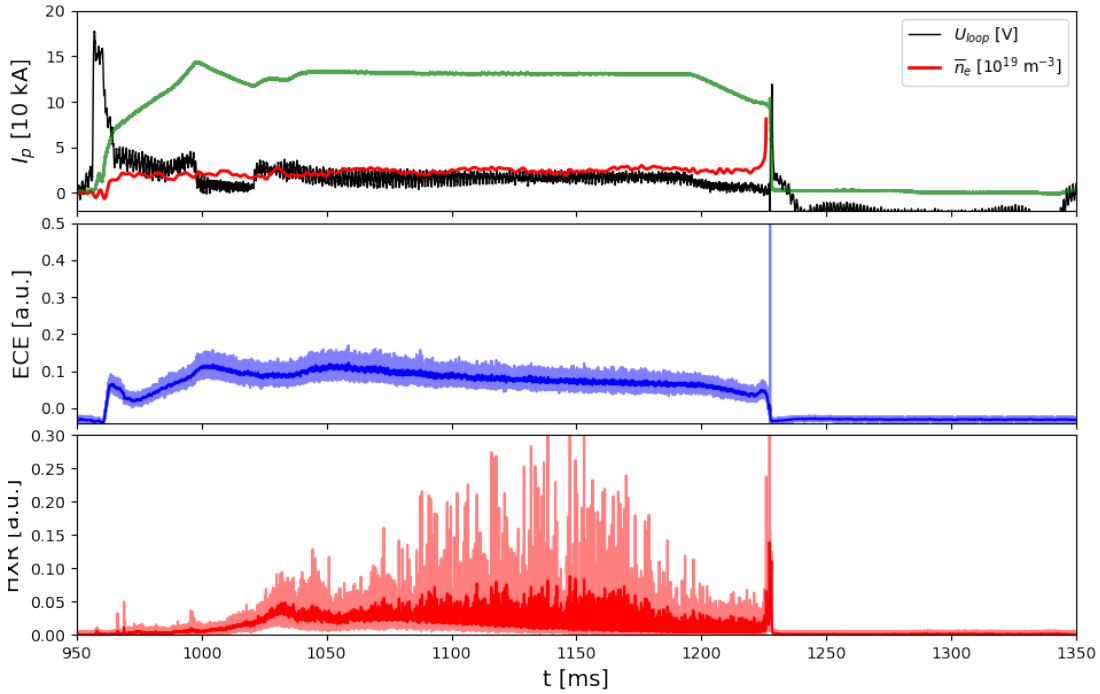

Fig. 3.12: Data from diagnostics, shot #13074. Lower number of the REs present in this discharge.

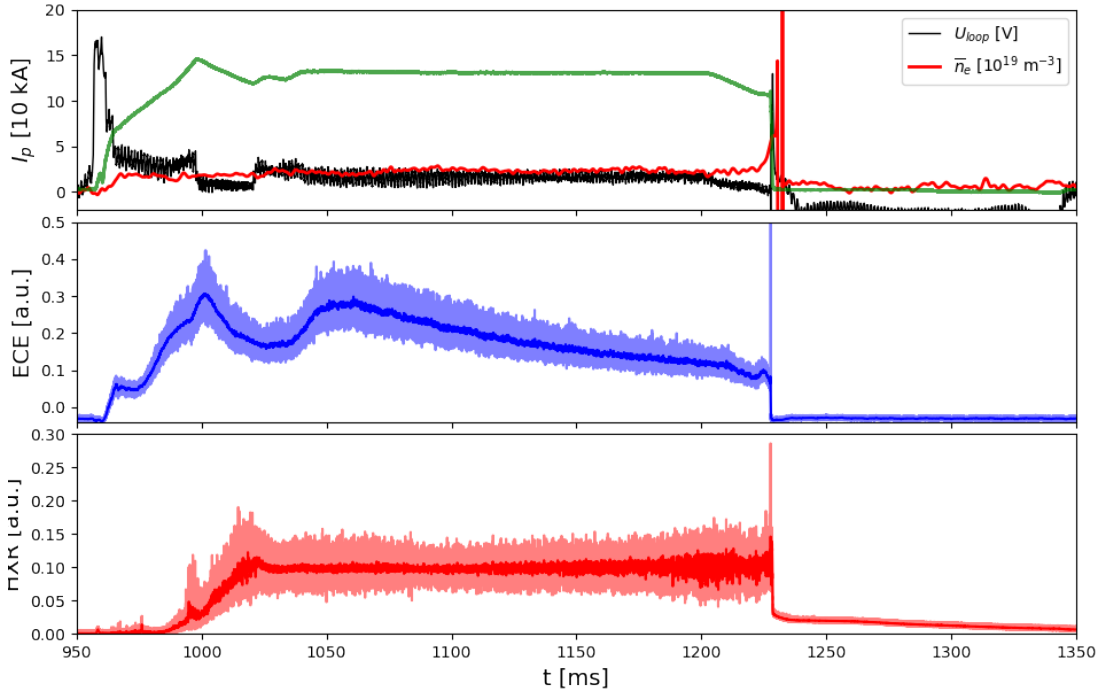

Fig. 3.13: Data from diagnostics, shot #13075. Regular discharge with high number of the REs.

Also measurements of the RE beam after argon MGI into rump-up phase are interesting. In some discharges filaments are visible in the RIS camera in Fig. 3.15, together with peaks in ECE and HXR signal in Fig. 3.14. Further analysis of the ECE and HXR signal shift have to be done to make general conclusions.

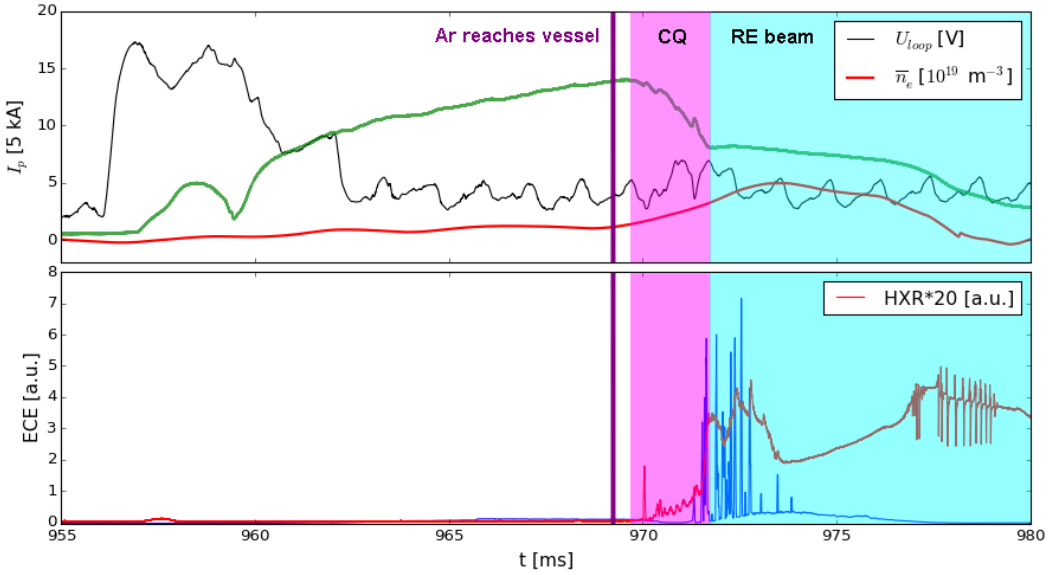

Fig. 3.14: Data from diagnostics, shot #13123. MGI disruption in rump-up phase and RE beam generation in 971 ms.

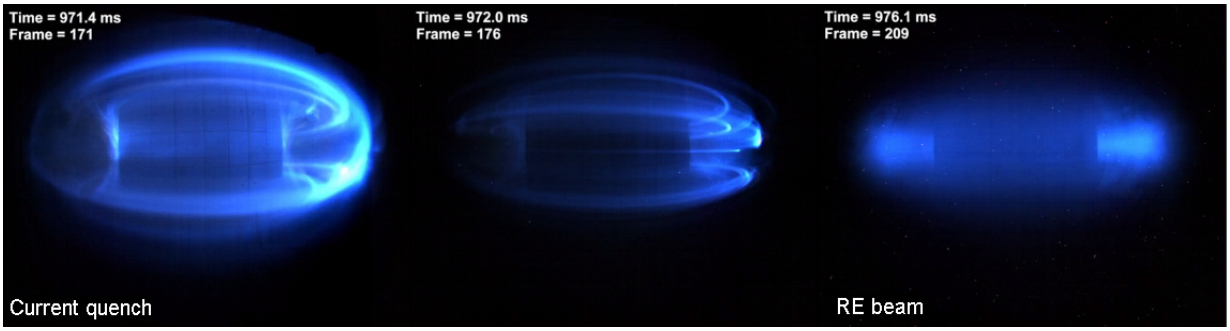

Fig. 3.15: Camera images of current quench and RE beam phase, shot #13123.

Summary

This research task deals with the electron cyclotron emission from non-thermal runaway electrons. A vertical ECE heterodyne radiometer was designed and utilized on the COMPASS tokamak, supported by numerical simulations. The main task was to determinate of the usability and reliability of the developed diagnostic.

The first chapter presents a very brief introduction to the runaway electron physics. It contains a summary of the runaway generation mechanisms and principal detection methods. The next topic, electron cyclotron emission theory, is described together with wave propagation in plasma and important equations useful for ray tracing.

The second chapter introduces experiments of non-thermal EC emission performed in TCV and Alcator C. Heterodyne COMPASS V-ECE radiometer technical specification is then presented. No calibration have been utilized yet.

The third section shows the principles of the SPECE code simulations and other calculations. The cutoff conditions were investigated. The ECE measurements are not infulenced by the cutoff limitations in discharges with average electron density below $3\dot{1}0^{19}$ m_{-3}. The E2-band (76−88 GHz) with extraordinary (X) polarisation is used. In the signal analysis we have to deal with the optically thin plasma. It is possible to measure non-thermal ECE from 3^{rd} and higher harmonic meaning the REs with the kinetic energy above 50 kEV.

The last section focuses on the first measurements. The list of scenarios in the runaway dedicated campaign is presented. We demonstrate that there is no unexpected signal in high-density discharges, in which cutoffs prevent ECE signal propagation. When the electron density drops below the cutoff limit our results indicate that we are able to measure runaway electron cyclotron emission. With the density far below cutoff condition we found ourselves in a situation when most probably the thermal emission from the 2^{nd} harmonic is measured.

Further plan for the diploma thesis is a full-wave reflection simulation usage to understand the beam behaviour in the tokamak. X-mode vs. O-mode measurements comparison could help to determine the optical depth role. The most advantageous feature would be radiometer intensity calibration and investigation of the RE dynamics.

References

[1] ITER web page. *What will ITER do?* http://www.iter.org/sci/Goals.

[2] R. Jaspers. *Relativistic Runaway Electrons Tokamak Plasmas*. Technische Universiteit Eindhoven, 1995. http://www.iaea.org/inis/collection/NCLCollectionStore/_Public/27/012/27012481.pdf.

[3] H. Knoepfel and D. A. Spong. Runaway electrons in toroidal discharges. *Nuclear Fusion*, 19(6):785–829, 1979. http://iopscience.iop.org/0029-5515/19/6/008.

[4] H. Dreicer. Electron and Ion Runaway in a Fully Ionized Gas. I. *Physical Review*, 115(2):238–249, 1959. https://journals.aps.org/pr/abstract/10.1103/PhysRev.115.238.

[5] H. Dreicer. Electron and Ion Runaway in a Fully Ionized Gas. II. *Physical Review*, 117(2):329–342, 1960. https://journals.aps.org/pr/abstract/10.1103/PhysRev.117.329.

[6] R. S. Granetz and B. et al. Esposito. An ITPA joint experiment to study runaway electron generation and suppression. *Physics of Plasmas*, 21(7), 2014. http://aip.scitation.org/doi/10.1063/1.4886802.

[7] O. Ficker. Generation , losses and detection of runaway electrons in tokamaks, 2015. https://physics.fjfi.cvut.cz/publications/FTTF/DP_Ondrej_Ficker.pdf.

[8] H. M. Smith and E. Verwichte. Hot tail runaway electron generation in tokamak disruptions. *Physics of Plasmas*, 15(7), 2008. http://aip.scitation.org/doi/10.1063/1.2949692.

[9] M. Rosenbluth and S. Putvinski. Theory for Avalanche of Runaway Electrons in Tokamaks. *Nuclear Fusion*, 37(10):1689–1699, 1997. http://iopscience.iop.org/0029-5515/37/10/I03.

[10] M. Bornatici, O. De Barbieri, and F. Engelmann. Electron Cyclotron Emission and Absorption in Fusion Plasmas. *Nuclear Fusion*, 23(9):1153–1257, 1983. http://iopscience.iop.org/article/10.1088/0029-5515/23/9/005/pdf.

[11] E. Mazzucato. *Electromagnetic waves for thermonuclear fusion research*. World Scientific, Singapore, 2014. http://scitation.aip.org/content/aip/journal/pofb/4/10/10.1063/1.860354i.

[12] I. H. Hutchinson. *Principles of Plasma Diagnostics*. Cambridge University Press, New York, 2002. http://iopscience.iop.org/article/10.1088/0741-3335/44/12/701/meta.

[13] T. H. Stix. *Waves in Plasma*. American Institute of Physics, New York, 1992.

[14] D. G. Swanson. *Series in Plasma Physics Plasma Waves*. IOP, Philadelphia, 2003.

[15] D. Farina, L. Figini, P. Platania, and C. Sozzi. SPECE: A code for electron cyclotron emission in tokamaks. In *AIP Conference Proceedings*, volume 988, pages 128–131, 2008. http://aip.scitation.org/doi/abs/10.1063/1.2905053.

[16] P. Blanchard and S. et al. Alberti. High field side measurements of non-thermal electron cyclotron emission on TCV plasmas with ECH and ECCD. *Plasma Phys. Control. Fusion*, 44(4402):2231–2249, 2002. http://iopscience.iop.org/0741-3335/44/10/310.

[17] K. Kato and I. H. Hutchinson. Alcator C vertical viewing electron cyclotron emission diagnostic. *Review of Scientific Instruments*, 57(8):1959–1961, 1986. http://aip.scitation.org/doi/abs/10.1063/1.1138806.

[18] K. Kato and I. H. Hutchinson. Nonthermal electron velocity distribution measured by electron cyclotron emission in Alcator C tokamak. *Physical Review Letters*, 56(4):340–343, 1986. https://journals.aps.org/prl/abstract/10.1103/PhysRevLett.56.340.

[19] D. R. Roberts and R. F. et al Steimle. Vertical viewing of electron-cyclotron emissions for diagnosing fast-electron dynamics in TEXT-U. *Review of Scientific Instruments*, 66(57):427–429, 1995. http://scitation.aip.org/content/aip/journal/rsi/66/1?ver=pdfcov.

[20] F. J. Stauffer and D. A. et al. Boyd. TFTR Michelson interferometer electron cyclotron emission diagnostic. *Review of Scientific Instruments*, 56(5):925–927, 1985. http://aip.scitation.org/doi/10.1063/1.1138044.

[21] J. Reed, S. Janz, R. Ellis, and John Lohr. Electron density measurements from cutoff of electron cyclotron emission in the DIII-D tokamak. *Review of Scientific Instruments*, 59(8):1608–1610, 1988. http://aip.scitation.org/doi/10.1063/1.1140162.

[22] J. Zajac, J. Preinhaelter, and J. et al. Urban. EBE/ECE Radiometry on COMPASS Tokamak—Design and First Measurements. In *AIP Conference Proceedings*, volume 1187, pages 473–476, 2009. http://proceedings.aip.org/proceedings/confproceed/1187.jsp.

[23] J. Zajac, J. Preinhaelter, and J. et al. Urban. Electron cyclotron-electron Bernstein wave emission diagnostics for the COMPASS tokamak. *Review of Scientific Instruments*, 81(10), 2010. http://aip.scitation.org/doi/10.1063/1.3475715.

[24] H. J. Hartfuss, T. Geist, and M. Hirsch. Heterodyne methods in millimetre wave plasma diagnostics with applications to ECE, interferometry and reflectometry. *Plasma Phys. Control. Fusion*, 39:1693–1769, 1997. http://iopscience.iop.org/article/10.1088/0741-3335/39/11/001/meta.

[25] J. Wesson and D. Campbell. *Tokamaks*. Oxford University Press, 2011, New York, 2011.